OPEN ACCESS



Deep Hubble Space Telescope Photometry of Large Magellanic Cloud and Milky Way Ultrafaint Dwarfs: A Careful Look into the Magnitude-Size Relation

Hannah Richstein ¹, Nitya Kallivayalil ¹, Joshua D. Simon ², Christopher T. Garling ¹, Andrew Wetzel ³, Jack T. Warfield¹, Roeland P. van der Marel^{4,5}, Myoungwon Jeon^{6,7}, Jonah C. Rose^{8,9}, Paul Torrey¹, Anna Claire Engelhardt¹⁰, Gurtina Besla¹¹, Yumi Choi¹², Marla Geha¹³, Puragra Guhathakurta¹⁴, Evan N. Kirby¹⁵, Ekta Patel¹⁶, Elena Sacchi^{17,18}, and Sangmo Tony Sohn⁴ Department of Astronomy, University of Virginia, 530 McCormick Road, Charlottesville, VA 22904 USA Observatories of the Carnegie Institution for Science, 813 Santa Barbara Street, Pasadena, CA 91101, USA ³ Department of Physics and Astronomy, University of California, One Shields Avenue, Davis, CA 95616, USA Space Telescope Science Institute, 3700 San Martin Drive, Baltimore, MD 21218, USA ⁵ The William H. Miller III Department of Physics & Astronomy, Bloomberg Center for Physics and Astronomy, Johns Hopkins University, 3400 N. Charles Street, Baltimore, MD 21218, USA ⁶ School of Space Research, Kyung Hee University, 1732 Deogyeong-daero, Yongin-si, Gyeonggi-do 17104, Republic of Korea Department of Astronomy & Space Science, Kyung Hee University, 1732 Deogyeong-daero, Yongin-si, Gyeonggi-do 17104, Republic of Korea Department of Astronomy, University of Florida, 211 Bryant Space Science Center, Gainesville, FL 32611, USA Center for Computational Astrophysics, Flatiron Institute, 162 Fifth Avenue, New York, NY 10010, USA Department of Physics and Astronomy, George Mason University, 4400 University Drive, MSN: 3F3, Fairfax, VA 22030, USA Steward Observatory, University of Arizona, 933 N. Cherry Avenue, Tucson, AZ 85719, USA

12 NOIRLab, 950 N. Cherry Avenue, Tucson, AZ 85719, USA ¹³ Department of Astronomy, Yale University, P.O. Box 208101, New Haven, CT 06520, USA ¹⁴ Department of Astronomy and Astrophysics, University of California Santa Cruz, University of California Observatories, 1156 High Street, Santa Cruz, CA 95064, USA ¹⁵ Department of Physics & Astronomy, University of Notre Dame, 225 Nieuwland Science Hall, Notre Dame, IN 46556, USA Department of Physics and Astronomy, University of Utah, 115 South 1400 East, Salt Lake City, UT 84112, USA Leibniz-Institut für Astrophysik Potsdam, An der Sternwarte 16, 14482 Potsdam, Germany ¹⁸ INAF-Osservatorio di Astrofisica e Scienza dello Spazio di Bologna, Via Gobetti 93/3, I-40129 Bologna, Italy

Abstract

Received 2024 February 12; revised 2024 March 28; accepted 2024 March 28; published 2024 May 20

We present deep Hubble Space Telescope photometry of 10 targets from Treasury Program GO-14734, including six confirmed ultrafaint dwarf (UFD) galaxies, three UFD candidates, and one likely globular cluster. Six of these targets are satellites of, or have interacted with, the Large Magellanic Cloud (LMC). We determine their structural parameters using a maximum-likelihood technique. Using our newly derived half-light radius (r_h) and V-band magnitude (M_V) values in addition to literature values for other UFDs, we find that UFDs associated with the LMC do not show any systematic differences from Milky Way UFDs in the magnitude–size plane. Additionally, we convert simulated UFD properties from the literature into the M_V - r_h observational space to examine the abilities of current dark matter (DM) and baryonic simulations to reproduce observed UFDs. Some of these simulations adopt alternative DM models, thus allowing us to also explore whether the M_V - r_h plane could be used to constrain the nature of DM. We find no differences in the magnitude–size plane between UFDs simulated with cold, warm, and self-interacting DM, but note that the sample of UFDs simulated with alternative DM models is quite limited at present. As more deep, wide-field survey data become available, we will have further opportunities to discover and characterize these ultrafaint stellar systems and the greater low surface-brightness universe.

Unified Astronomy Thesaurus concepts: Dwarf galaxies (416); HST photometry (756); Galaxy structure (622); Local Group (929)

1. Introduction

Within the cosmological paradigm of cold dark matter (CDM), structures in the Universe that we observe today were formed through hierarchical evolution (e.g., White & Rees 1978; Peebles 1984; Frenk et al. 1988). The most massive dark matter (DM) halos grew by accreting less massive objects, a phenomenon that has left evidence in many forms, such as galaxy clusters and the satellite population of our own Milky Way (MW). While the two most massive satellites of the MW, the Large Magellanic Cloud (LMC) and Small Magellanic

Original content from this work may be used under the terms of the Creative Commons Attribution 4.0 licence. Any further distribution of this work must maintain attribution to the author(s) and the title of the work, journal citation and DOI.

Cloud, have been known for millennia, the advent of wide-field optical imaging surveys with digital CCD detectors has enabled the discovery of dwarf satellites orders of magnitude fainter than the Magellanic Clouds.

Among these galaxies are ultrafaint dwarfs (UFDs), which were first discovered after the Sloan Digital Sky Survey began (e.g., Willman et al. 2005), and over 60 candidates have been discovered since (e.g., Belokurov et al. 2006; Koposov et al. 2015a; Laevens et al. 2015b; Bechtol et al. 2015; Drlica-Wagner et al. 2015; Kim & Jerjen 2015; Torrealba et al. 2016a; Homma et al. 2016). While UFDs seem to be an extension of classical dwarf galaxies ($M_{\star} \approx 10^{5-7} M_{\odot}$), as a subclass, they have been defined as having $L \leq 10^5 L_{\odot}$ and $M_{\star} \approx 10^{2-5} M_{\odot}$ (e.g., Bullock & Boylan-Kolchin 2017; Simon 2019). UFDs have the oldest, least chemically enriched stellar populations and could be the "fossils" of the first galaxies, having formed at

least $\sim 80\%$ of their stellar mass by the end of reionization ($z \sim 6$; Madau & Dickinson 2014) with little-to-no star formation activity since (e.g., Bovill & Ricotti 2009; Brown et al. 2014; Weisz et al. 2014; Sacchi et al. 2021).

The infall history of these UFDs is encoded in their present-day dynamics. While some information can be extracted with only line-of-sight velocities (e.g., Rocha et al. 2012; Carlin et al. 2019; Garling et al. 2020), full 6D kinematics like those provided by the Gaia mission (Gaia Collaboration et al. 2016) allow for full orbital reconstruction (e.g., McConnachie & Venn 2020; Battaglia et al. 2022; Pace et al. 2022). This in turn allows us to search for signatures of group infall. With Gaia proper motions (PMs), a subset of UFDs have been linked kinematically with the LMC (e.g., Kallivayalil et al. 2018; Erkal & Belokurov 2020; Patel et al. 2020), and could thus be considered "satellites of satellites." These UFDs have occupied a different environment than the non-LMC associated dwarf galaxies for much of their existence.

For example, the LMC-associated UFDs had been in proximity to a moderately massive ($\gtrsim 10^{11} M_{\odot}$) galaxy before their infall into the MW halo. Additionally, with the LMC being on its first infall (e.g., Besla et al. 2007; Kallivayalil et al. 2013), these satellites may have been farther away from the proto-MW during the epoch of reionization ($z \sim 6$) than the MW satellites that were captured prior to the LMC's infall. Both sets (the non-LMC-associated and LMC-associated) of UFDs would have been distant enough to be at least outside the virial radius of the MW (Wetzel et al. 2015; Santistevan et al. 2023).

While essentially all UFDs appear to have formed the majority of their present-day stellar mass by the end of reionization (e.g., Brown et al. 2014; Weisz et al. 2014), UFDs that inhabited different environments during reionization could have different quenching times due to the inhomogeneity of reionization (Dawoodbhoy et al. 2018; Ocvirk et al. 2020; Sorce et al. 2022; Kim et al. 2023). As such, comparing the star formation histories (SFHs) of UFDs that inhabited different environments during reionization could offer insights into this epoch. Splitting the UFDs into subgroups based on their LMC association, Sacchi et al. (2021) found tantalizing signs of differences in the SFHs. The LMC-associated UFDs continued forming stars for, on average, more than 500 Myr after the non-LMC-associated galaxies had completed their star formation. This could hint at the galaxies' early environment having an impact on their evolution.

There are some properties of galaxies that we might expect to be largely invariant to the environment and more dependent on DM halo mass. For example, the existence of a stellar-to-halo-mass relation has been well established (e.g., Behroozi et al. 2010). However, for halo masses below $\sim 10^{10} M_{\odot}$, the relation has been more difficult to characterize (e.g., Brook et al. 2014; Garrison-Kimmel et al. 2014, 2017; Read et al. 2017; Munshi et al. 2021). It is not immediately clear then, whether equal mass halos in an LMC versus MW environment would (without any disruptive events) evolve to host galaxies of similar stellar mass. Stellar mass is inferred from a galaxy's luminosity, but with such a small sample size, it could be difficult to interpret how meaningful the differences between populations are.

The goal of this study is thus twofold: (1) to compare LMC and MW UFDs in an observed space, namely the absolute magnitude (M_V) versus half-light radius (r_h) plane, and (2) to

explore whether simulated UFDs can offer insights about what we observe and what we might expect to observe as newer facilities come online. While reviewing the state of simulated UFDs, we also compare simulation results from baryonic runs based on alternative DM models, particularly as they relate to predictions of cored or cuspy density profiles.

The "core-cusp" problem arose from the mismatch of the predicted "cuspy" density profiles from cold DM-only simulations and the implied "cored" profiles from observed rotation curves (e.g., Flores & Primack 1994; Moore 1994), and has been one of the classical challenges to the CDM model (see, e.g., Bullock & Boylan-Kolchin 2017; Sales et al. 2022, for a review). While solutions have since been presented that are consistent with CDM (e.g., Navarro et al. 1996; Gelato & Sommer-Larsen 1999; Read & Gilmore 2005; Oh et al. 2011; Pontzen & Governato 2012; Chan et al. 2015; Lazar et al. 2020; Orkney et al. 2021), we take this opportunity to examine and compare the predictions coming from alternative DM models on UFD mass scales.

Here, we choose to revisit the seven targets from Sacchi et al. (2021)—Horologium I (Hor I), Hydra II (Hya II), Phoenix II Sagittarius II Reticulum II (Ret II), (Phe II), Triangulum II (Tri II), and Tucana II (Tuc II)—as well as add three additional targets from the Hubble Space Telescope (HST) Treasury Program GO-14734 (PI: N. Kallivayalil) that could be associated with the LMC: Grus II (Gru II), Horologium II (Hor II), and Tucana IV (Tuc IV; Battaglia et al. 2022; Correa Magnus & Vasiliev 2022). We note that Hor II has not been spectroscopically confirmed to be a DM dominated galaxy and that Sgr II is most likely a globular cluster (Longeard et al. 2021; Baumgardt et al. 2022). We include Sgr II to remain consistent with the original Sacchi et al. (2021) sample and will refer to all of the included targets as UFDs for ease of discussion.

The structure of this paper is as follows. In Section 2, we describe the observations and photometry process. In Sections 3 and 4, we discuss our methods of structural analysis and absolute magnitude calculations, then examine our results in the context of past literature. Section 5 includes our comparison of LMC-associated and non-LMC associated UFDs, as well as a comparison of observed and simulated UFDs. We conclude in Section 6.

2. Photometry of Hubble Space Telescope Data

2.1. Target Selection

As explained above, we have chosen to study the seven UFDs whose SFHs were characterized in Sacchi et al. (2021). In that work, the seven UFDs were separated into LMC (Hor I, Phe II, Ret II) and non-LMC associated UFDs (Hya II, Sgr II, Tri II, Tuc II) on the basis of orbit models (Patel et al. 2020) constructed with Gaia DR2 PMs for the UFDs (Kallivayalil et al. 2018; Erkal & Belokurov 2020). Previous studies (e.g., Jethwa et al. 2016; Sales et al. 2017) also supported some of these classifications, but where there were disagreements, the results of Patel et al. (2020) were adopted as they used the most updated PM information (Gaia DR2) available at the time.

Since then, Battaglia et al. (2022), Correa Magnus & Vasiliev (2022), and Pace et al. (2022), among others, have published studies using Gaia eDR3 (Gaia Collaboration et al. 2021) to improve the PM measurements and orbital models for several of these UFDs. Battaglia et al. (2022) support the

Table 1
Summary of Primary ACS Observations and Field Completeness

Satellite Name	UT Date	Filter	Exposure Time (s)	50% (VegaMag)	90% (VegaMag)
Grus II (Gru II)	2016 Nov 02	F606W	4 × 1130	27.8	27.0
	2016 Oct 08	F814W	4×1130	26.8	26.0
Horologium I (Hor I)	2017 Jul 31	F606W	4×1131	27.8	27.0
	2017 Aug 01	F814W	4 × 1131	26.8	26.0
Horologium II East (Hor II)	2016 Sep 26	F606W	4 × 1131	28.1	27.3
	2016 Sep 26	F814W	4 × 1131	27.1	26.3
Horologium II West (Hor II)	2017 Mar 22	F606W	4 × 1131	28.0	27.2
	2017 Mar 22	F814W	4×1131	27.0	26.2
Hydra II (Hya II)	2016 Dec 13	F606W	4×1186	27.6	26.9
	2016 Dec 16	F814W	4×1186	26.6	25.9
Phoenix II (Phe II)	2017 May 08	F606W	4 × 1131	27.8	27.0
	2017 May 08	F814W	4 × 1131	26.8	26.0
Reticulum II (Ret II)	2017 Nov 18	F606W	4×1145	27.4	26.2
	2017 Nov 28	F814W	4×1145	26.4	25.2
Sagittarius II (Sgr II)	2016 Oct 19	F606W	4×1127	27.5	26.8
	2016 Oct 01	F814W	4×1127	26.8	26.1
Triangulum II East (Tri II)	2016 Dec 31	F606W	4×1137	27.7	27.0
	2016 Dec 03	F814W	4×1137	26.7	26.0
Triangulum II West (Tri II)	2017 Jun 22	F606W	4×1137	27.7	26.9
	2017 Jun 22	F814W	4×1137	26.7	25.9
Tucana II Northeast (Tuc II)	2017 Jun 27	F606W	4×1138	28.1	27.3
	2017 Jun 29	F814W	4×1138	27.1	26.3
Tucana II Northwest (Tuc II)	2017 Aug 26	F606W	4×1138	27.9	27.1
	2017 Aug 31	F814W	4×1138	26.9	26.1
Tucana II Southeast (Tuc II)	2017 Aug 21	F606W	4×1138	28.0	27.2
	2017 Aug 25	F814W	4×1138	27.0	26.2
Tucana II Southwest (Tuc II)	2018 Mar 01	F606W	4×1138	27.5	26.7
	2018 Mar 03	F814W	4 × 1138	26.5	25.7
Tucana IV North (Tuc IV)	2017 Apr 06	F606W	4×1140	28.0	27.3
	2017 Apr 06	F814W	4×1140	27.0	26.3
Tucana IV South (Tuc IV)	2016 Sep 28	F606W	4×1140	27.9	27.2
	2016 Sep 28	F814W	4×1140	26.9	26.2

classification of Hor I, Phe II, and Ret II as "highly likely former satellites of the LMC," and add Hor II and Tuc IV as "potential" former satellites and Gru II as a recently captured LMC satellite. Correa Magnus & Vasiliev (2022) also present orbital models, which suggest Tuc IV and Gru II were recently captured by the LMC, while Hor II and Ret II only show a moderate likelihood of having been associated with the LMC in the past. Other suspected/confirmed LMC satellites include Carina II, Carina III, and Hydrus I (Kallivayalil et al. 2018; Erkal & Belokurov 2020; Patel et al. 2020; Battaglia et al. 2022; Correa Magnus & Vasiliev 2022); however, we do not present photometry for them here as they were not observed as part of the Treasury program. Our final groupings include Gru II, Hor I, Hor II, Phe II, Ret II, and Tuc IV as LMCassociated UFDs and Hya II, Sgr II, Tri II, and Tuc II as non-LMC-associated UFDs.

2.2. Observations and Reduction

All 10 targets (Table 1) were observed in the F606W and F814W filters of the HST Advanced Camera for Surveys (ACS; Ford et al. 1998) using the Wide Field Channel (WFC). Off-target fields were simultaneously observed with the UV/visible channel (UVIS) of the Wide Field Camera 3 (WFC3) in order to characterize the stellar background/foreground distributions. Each ACS/WFC field of view (FOV) is 202" × 202", while the WFC3/UVIS off-fields are 162" × 162". The ACS data used in

this paper can be found in the Mikulski Archive for Space Telescopes (MAST) doi:10.17909/tvwk-ye33. As these observations were planned as first epochs for follow-up PM measurements, each target field had four dithered exposures in order to facilitate well-sampled templates for background galaxies. These were taken using two orbits in each filter, with an integration time per exposure of approximately one half-orbit (~1100 s). Table 1 gives the average exposure time in integer seconds for each target. Hor II, Tri II, and Tuc IV had two pointings, while Tuc II had four pointings, so as to ensure there were enough stars for robust PM measurements.

The individual dither (flc) images were downloaded from MAST, having already been processed and corrected for charge transfer inefficiency using the current ACS and WFC3 pipelines (Anderson & Ryon 2018; Anderson et al. 2021). The four separate dithers from each filter were aligned to each other using TweakReg and then combined using the DRIZZLE algorithm (Fruchter & Hook 2002) as implemented by the HST software DRIZZLEPac (STScI Development Team 2012; Avila et al. 2015) to create drc fits files. The segmentation routine from photutils was used to identify and mask the chip gaps, detector artifacts, and large saturated sources.

2.3. DAOPHOT-II

The photometry will be described in detail in the data paper accompanying the public release of the point-spread function (PSF)-fit source catalogs (H. Richstein et al., 2024, in preparation). We provide a brief overview here.

PSF-fitting photometry was performed on the masked drc files using DAOPHOT-II and ALLSTAR (Stetson 1987, 1992). The source lists from F606W and F814W were matched using DAOMATCH and DAOMASTER to create a preliminary PSF source catalog. To calibrate our photometry, we first removed DAOPHOT's intrinsic zero-point of 25 mag, then added appropriate VegaMag zero-points (from the ACS Zero-point Calculator for ACS and stsynphot for WFC3) corrected for the exposure times of our images.

The PSF magnitudes are computed within a finite radius, so to correct for the infinite aperture case, we applied an aperture correction. To calculate this, we performed aperture photometry on the same drc images using the photutils (Bradley et al. 2020) routines DAOStarFinder and aperture_photometry. We used an aperture with a radius of 0.12 and applied the VegaMag zero-points and encircled energy corrections from Bohlin (2016) and Medina et al. (2022) for ACS and WFC3/UVIS, respectively. The F606W and F814W aperture source lists were then matched to each other to create an aperture photometry catalog. Sources were matched between the PSF and aperture photometry catalogs to determine an aperture correction that was then applied to the DAOPHOT PSF-derived VegaMag magnitudes.

2.4. Artificial Star Tests and Flag Creation

To determine our photometric completeness limits, photometric error functions, and to aid in developing metrics for star-galaxy separation, we performed artificial star tests (ASTs) with the ADDSTAR function of DAOPHOT. For each filter and pointing, we inject 500 artificial stars into the science image at a time in order to avoid changing the total source density of the frame significantly. After injecting the artificial stars, we performed the same ALLSTAR photometry as on the masked drc files. We performed this process 500 times so that we had a total of 250,000 artificial stars per filter and pointing.

A primary source of contamination in deep photometric studies of MW dwarf satellites is faint, unresolved background galaxies. As such, essentially all downstream analyses (e.g., measuring structural parameters) rely on methods to exclude these contaminants in order to obtain a highly pure sample of stars in the dwarf galaxy of interest. We created a flag to distinguish between stars and galaxies based on the standard error (ERR), SHARP, and CHI parameters of stars recovered from the ASTs. The DAOPHOT ERR value is an estimate of the star's ERR, which takes into account the flux, PSF residuals, and noise properties of the images. SHARP and CHI are quality diagnostics relating how the model PSF compares to each source.

The SHARP value of an isolated star should be close to zero, while more extended objects would have SHARP values much greater than zero, and image defects and cosmic rays would have values much less than zero. The CHI value represents the ratio between the pixel-to-pixel scatter in the PSF residuals and the scatter expected from the image noise properties. Stars should scatter around unity, although brighter stars may have higher values due to saturation effects.

We used exponential functions to divide between acceptable and poor parameter values. To begin, we binned the artificial star parameters in magnitude space, then calculated the median values across the bins. To account for the spread in parameter space of the observed stars, we added the 3σ of each bin to its

respective median, and then fit an exponential function to those values. For the SHARP parameter, we fit two functions, as there was a spread in both the positive and negative direction. For the negative function, we subtracted instead of added the 3σ .

We assigned sources their flag values (between 0 and 1, inclusive) based on where their SHARP, ERR, and CHI values fell in relation to the functional fits. The ERR and CHI functions acted as upper limits, while the source's SHARP value had to fall between the positive and negative function lines to count as meeting the criteria. If a source met the SHARP and ERR criteria in both F606W and F814W, it was assigned a 1. If sources did not meet these criteria in both filters, but did meet at least the SHARP and ERR criteria in the same filter and the CHI criterion in either filter, they were assigned flag values between 0.5 and 1 (exclusive). For this analysis, we only considered sources with flag values greater than 0.5.

2.5. Color-Magnitude Diagrams

The color-magnitude diagrams (CMDs) for each target are shown in Figure 1. Here, they have been transposed to absolute magnitude space by applying the dust correction and subtracting the distance modulus listed in Table 2. To correct for the reddening and dust extinction, we used the Schlegel et al. (1998) maps within the dustmaps module (Green 2018) and applied the Schlafly & Finkbeiner (2011) recalibration. The correction was calculated for each individual star based on its R.A. and decl. values. The sources plotted in the CMDs are those above the 90% completeness limit and with flag values above 0.5. We additionally applied a straight (vertical) colorcut in CMD space tailored to each target for background galaxy removal, and have highlighted the likely member stars in black. We leave the foreground/background sources that pass our color-cut, as the code that we use for fitting structural parameters can account for a foreground/background term. The lack of bright red giant branch (RGB) stars in some of the CMDs (e.g., Ret II, Tri II) is due to saturation in the images.

3. Structural Analysis

In the years following the discovery of the first UFDs, it became important to quantify how well one could actually describe the morphology of such diffuse objects. In a comprehensive exploration of systematics that affect the measurement of dwarf morphologies with resolved stars, Muñoz et al. (2012) found three aspects of observational design that influence the measurement accuracy. They found that morphologies are best measured with observations covering a large FOV (>3 times the galaxy half-light radius) to sufficient depth to both achieve a central density contrast (relative to the background and foreground contamination) of \sim 20 and to measure as many stars in the dwarf as possible (preferably >1000).

In practice, ground-based observatories with large fields of view can achieve sufficient depths to robustly measure the morphologies of the brighter and closer MW satellites. However, for the faintest and farthest UFDs, these observatories can be limited by the photometric depth that they can achieve and their ability to achieve good enough seeing for confident star–galaxy separation. Although its FOV is limited, HST/ACS can thus have an advantage in this regime for its superior photometric depth and image resolution, which allows for better star–galaxy separation and lower background levels.

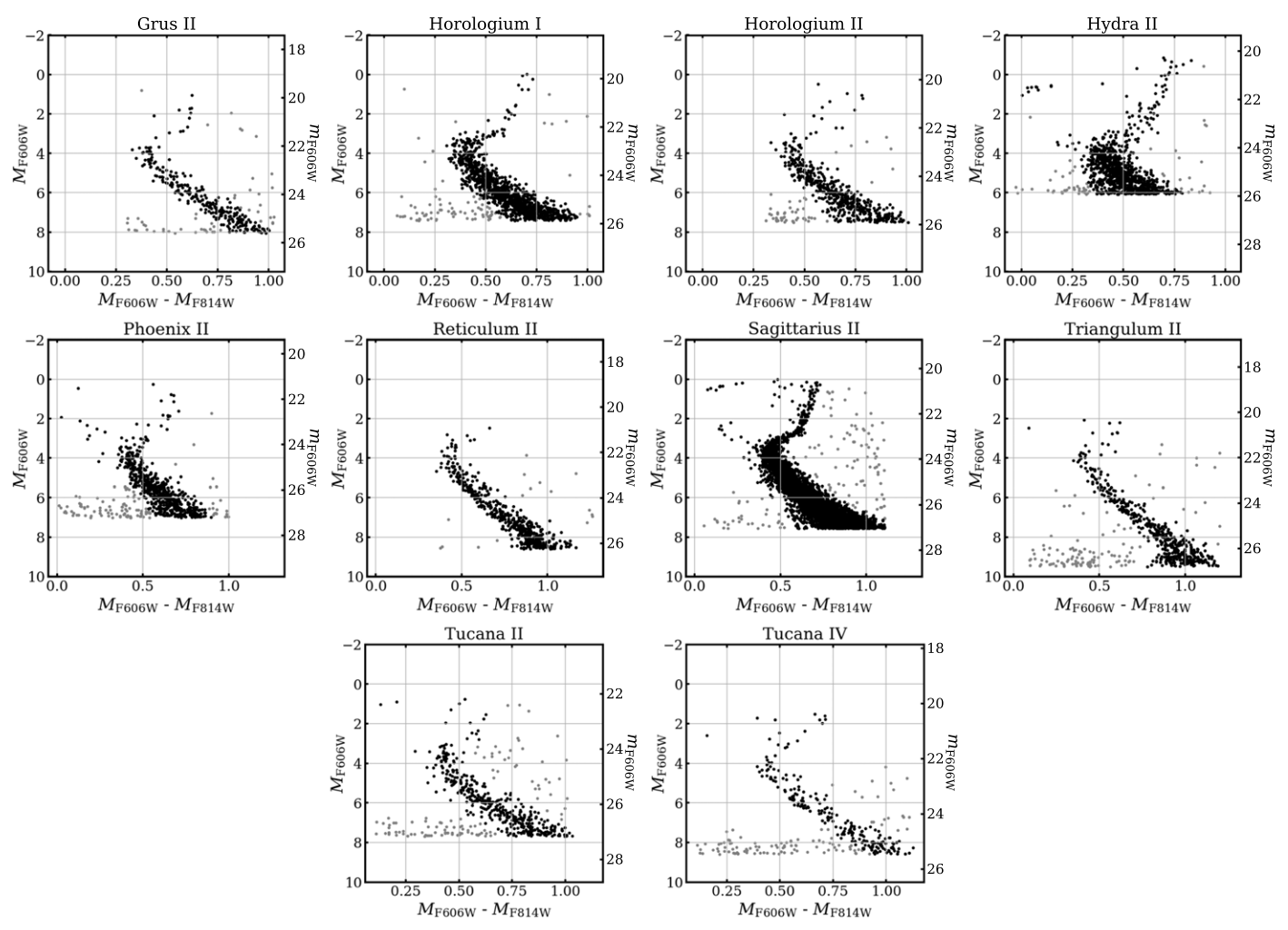


Figure 1. Color-magnitude diagrams in the VegaMag system for the 10 targets presented herein. The sources presented are all sources that passed the quality, completeness, and color-cuts imposed for the morphological analysis. We have colored in gray the sources that are most likely background/foreground contamination but are used in the structural fitting to determine the background parameter.

With the available HST pointings, we are able to measure structural parameters for six of the 10 targets: Hor I, Hor II, Hya II, Phe II, Sgr II, and Tri II. For Gru II, Ret II, Tuc II, and Tuc IV, our imaging covers only between $\sim\!\!0.5$ and $1\times$ the half-light radii of these objects, preventing us from making reliable morphological measurements.

3.1. Fitting 2D Profiles

We employed the same technique used in Drlica-Wagner et al. (2020) and Simon et al. (2021) that was based on the maximum-likelihood algorithm presented in Martin et al. (2008) to fit 2D profiles of each galaxy. For each target, we modeled both an exponential and a Plummer (Plummer 1911) profile, then performed binned Poisson maximum-likelihood fits to the probability density functions. We had seven free parameters: center position (x_0, y_0) , number of stars (richness), 2D projected semimajor axis of the ellipse containing one-half the surface density of the galaxy (elliptical half-light radius; a_h), ellipticity (ϵ) , position angle of the semimajor axis measured from north through east (θ) , and foreground/

background surface density (average density of star-like sources in the FOV not belonging to the galaxy; Σ_h).

As we noted in Richstein et al. (2022), much of the past literature (e.g., Martin et al. 2008; Muñoz et al. 2018) reporting structural parameters has used r_h when referring to the elliptical half-light radius, although r_h has also been used to report azimuthally averaged half-light radius values (equal to $a_h \sqrt{1 - \epsilon}$; e.g., Drlica-Wagner et al. 2015). Thus, we choose to make the distinction here, and in our tables of past measurements, we use a_h for measured elliptical half-light radii. We use r_h as the azimuthally averaged half-light radius in our later comparison to simulations.

We divided the ACS FOV into 4.55×4.55 bins and applied masks to account for the ACS chip gap, saturated foreground stars, and extended, resolved background galaxies and to match the mask applied during the photometry process. We counted the stars in each bin and used the Markov Chain Monte Carlo ensemble sampler emcee (Foreman-Mackey et al. 2013) to sample the posterior probability distribution. We refer the reader to Richstein et al. (2022) for the explicit functional forms²¹ used for the exponential and Plummer profiles. Figure 2 shows an example corner plot (Foreman-

¹⁹ Similar to past morphology studies (e.g., Martin et al. 2008), assuming there is no mass segregation, the half-density and half-light radii are equivalent.

²⁰ Ellipticity is defined as $\epsilon = 1 - b/a$, where a and b are the lengths of the semimajor and semiminor axes, respectively.

 $[\]overline{^{21}}$ We note that the in-text equation for r_e in Richstein et al. (2022; Section 3.1) should be $r_e = a_h/1.68$.

Table 2
Adopted and Derived Parameters for the 10 Targets

	Adopted and Derived Parameters								
Parameter	$(m-M)_0^a$ (mag)	Distance (kpc)	$\sigma_v^{\text{b,c}}$ (km s ⁻¹)	r _h (arcmin)	<i>r_h</i> (pc)	m_V (mag)	$M_{1/2} \ (10^6 M_{\odot})$	$(M/L_V)_{1/2} \ (M_{\odot}/L_{\odot})$	References
Hor I	19.5 ± 0.2	79+8	$4.9^{+2.8}_{-0.9}$	1.46 ± 0.14	34+5	$16.12^{+0.06}_{-0.09}$	$0.88^{+1.2}_{-0.35}$	890+1200	1, 2
Hor II	19.46 ± 0.2	78^{+8}_{-7}		1.43 ± 0.17	32 ± 5	17.39 ± 0.10			3
Hya II	20.64 ± 0.16	134 ± 10	<3.6, <4.5	$2.26^{+0.37}_{-0.34}$	88^{+16}_{-14}	$15.80^{+0.11}_{-0.22}$	< 2.0	<670	4, 5
Phe II	$19.85^{+0.16}_{-0.17}$	93 ± 7	11.0 ± 9.4	$1.18^{+0.20}_{-0.18}$	32^{+6}_{-5}	$17.00^{+0.13}_{-0.09}$	$4.8^{+11.6}_{-3.7}$	$7800^{+18,000}_{-6500}$	6, 7
Sgr II	19.2 ± 0.2	69^{+7}_{-6}	1.7 ± 0.5	$1.82^{+0.08}_{-0.09}$	37 ± 4	$13.82^{+0.06}_{-0.04}$	$0.10^{+0.07}_{-0.05}$	17^{+12}_{-8}	8, 9
Tri II	17.27 ± 0.11	28^{+2}_{-1}	<3.4, <4.2	$3.34^{+0.60}_{-0.61}$	28 ± 5	$15.97^{+0.23}_{-0.25}$	< 0.48	<3200	10, 11
Gru II	18.71 ± 0.1	55 ± 3	<1.9, <2.0	$5.24^{+0.50}_{-0.48}$	84 ± 9	•••	< 0.35	<330	12, 13
Ret II	17.5 ± 0.1	32^{+2}_{-1}	$2.97^{+0.43}_{-0.35}$	$3.98^{+0.53}_{-0.57}$	37 ± 5		$0.48^{+1.5}_{-1.1}$	640^{+200}_{-150}	8, 14
Tuc II	18.8 ± 0.2	58^{+6}_{-5}	$3.8^{+1.1}_{-0.7}$	$9.83^{+1.66}_{-1.11}$	170^{+37}_{-33}		$2.9^{+2.0}_{-1.1}$	2100^{+1400}_{-780}	1, 15
Tuc IV	$18.36^{+0.18}_{-0.19}$	47 ± 4	$4.3_{-1.0}^{+1.7}$	$7.26^{+1.14}_{-0.88}$	100^{+17}_{-15}		$2.2^{+1.8}_{-1.1}$	3100^{+2900}_{-1600}	13

Notes. For each target, we list the distance modulus and velocity dispersion values from the literature. For the first six targets, we also list the azimuthally averaged r_h in arcminutes and parsecs, as well as our derived apparent and absolute V-band magnitudes. We list the dynamical mass within the 2D projected a_h ($M_{1/2}$) and mass-to-light ratio ((M/L_V)_{1/2}) derived using our r_h and M_V values. For the last four rows, we list the literature properties for the targets that we were unable to measure. ^a Koposov et al. (2015b) state that the uncertainties on their distance moduli are 0.1–0.2. We adopt 0.2 in our analysis.

References. (1) Koposov et al. (2015b); (2) Koposov et al. (2015a); (3) Kim & Jerjen (2015); (4) Martin et al. (2015); (5) Kirby et al. (2015b); (6) Nagarajan et al. (2022); (7) Fritz et al. (2019); (8) Mutlu-Pakdil et al. (2018); (9) Longeard et al. (2021); (10) Carlin et al. (2017); (11) Kirby et al. (2017); (12) Martínez-Vázquez et al. (2019); (13) Simon et al. (2020); (14) Ji et al. (2023); (15) Chiti et al. (2023).

Mackey 2016) with the posterior distributions for the exponential fit to Hor I. The corner plots for the exponential fits of the other targets are shown in Appendix A.

We see three different correlations between pairs of parameters: richness and background, a_h and background, and richness and a_h . These relations come from the finite number of stars used in the fit. For example, richness and background counts both depend on whether individual stars are considered to be contributing to the surface density of the galaxy or not. If more stars belong to the galaxy, the richness will increase, and the background will be lower. Similarly, a higher richness correlates with a larger a_h , as a greater number of stars at extended distances from the center would be considered part of the galaxy. This a_h and richness correlation also explains the a_h and background anticorrelation, as a larger a_h with a higher richness necessitates fewer stars belonging to the background.

As shown in Wheeler et al. (2019), measuring dwarf morphologies from shallow imaging with surface-brightness limits <30 mag arcsec $^{-2}$ can bias size measurements toward being too compact. For typical dwarfs in our sample, we are able to trace their light profiles to \sim 31.2 mag arcsec $^{-2}$ such that we should experience no significant bias in our morphological measurements from our surface-brightness limits. It is more common in our measured sample to be limited by our imaging FOV, as our imaging for some objects does not meet the recommended coverage of 3 times the a_h (Muñoz et al. 2012).

3.2. Apparent and Absolute V-band Magnitude Calculations

To calculate integrated magnitudes, we transformed the extinction-corrected F606W and F814W VegaMag values to V and I band, respectively. For the ACS photometry, we used the Sirianni et al. (2005) conversions, and for the WFC3 values, we used the coefficients from Harris (2018).

We applied the same probabilistic model used in Richstein et al. (2022) to integrate the magnitudes. Briefly, this entailed creating a Gaussian kernel (for both the ACS and WFC3 fields) with scikitlearn (Pedregosa et al. 2011) Kernel Density and fitting it to the stars in CMD space. Random samples were generated from these kernels, and the loglikelihood of each sample was computed with respect to the binned CMD data. We calculated excess flux from nonmember sources using a probabilistic background model created from the WFC3 field. The stellar density was determined by multiplying the log-likelihoods by the area of the CMD box and subtracting the off-field (WFC3) model from the on-field (ACS) model. The integral returned the flux of the stars inside the CMD box, which we multiplied by a correction factor to account for the flux outside the FOV. We converted this flux into magnitude space, giving the integrated apparent magnitude (m_V) .

We performed this calculation within a Monte Carlo simulation to include magnitude errors of the individual sources and the uncertainties on the FOV correction incorporating different model parameters. The median integrated m_V values are presented in Table 2. To calculate the absolute integrated magnitude (M_V) , we ran the same Monte Carlo simulation but included the distance modulus and its associated uncertainty.

As our methodology for measuring the integrated magnitudes of our galaxies does not account for the luminosity from stars fainter than our observational completeness limits, we are likely underestimating the total luminosity of our targets. Using a stellar luminosity function constructed by combining the Kroupa (Kroupa 2001) initial mass function with a 12 Gyr, [Fe/H] = -2.2 PARSEC (Bressan et al. 2012; Chen et al. 2014; Marigo et al. 2017) isochrone, we estimate that, for the targets considered here, we are missing between 1% and 10% of their total luminosities with an average of

b Kirby et al. (2015b, 2017) report their 90% and 95% confidence levels for the velocity dispersions.

^c Simon et al. (2020) report the 90% and 95.5% confidence upper limits on the velocity dispersion.

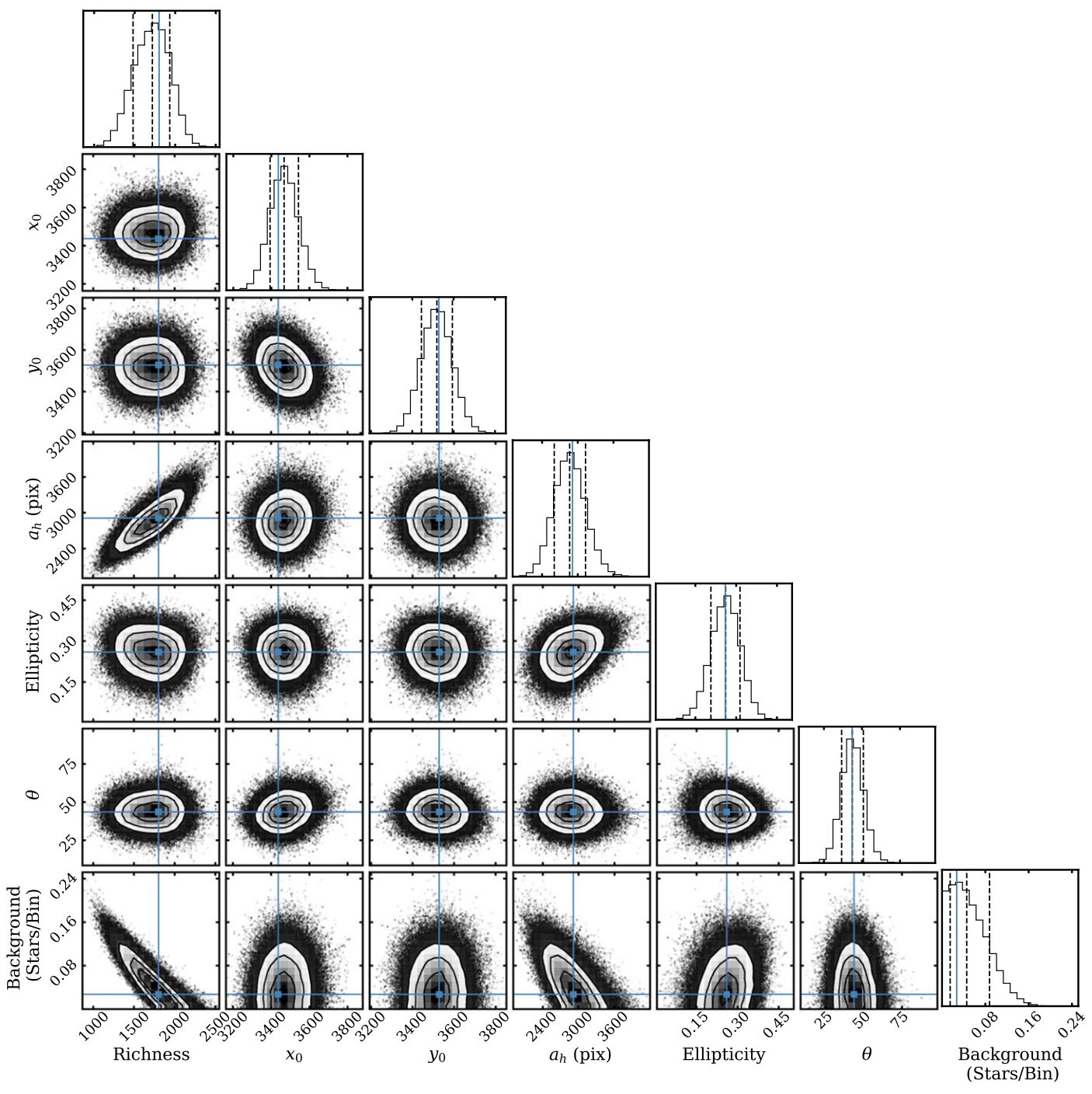


Figure 2. The posterior distributions of the seven-parameter structural fit for Hor I using the exponential model. The three black vertical dashed lines represent the 16th, 50th, and 84th percentiles. The blue lines and markers show the maximum-likelihood values.

 $\sim\!\!3\%$. This indicates that our integrated magnitudes may be biased fainter by at most $\sim\!\!0.1\,\mathrm{mag}$ due to our photometric completeness limits. The other sources of uncertainty (FOV correction, distance) thus dominate the reported uncertainties.

3.3. Mass-to-Light Ratios

We used our measured elliptical half-light radii to calculate updated mass estimates with velocity dispersion values (σ_{ν}) coming from the literature (see Table 2). We employed the

Wolf et al. (2010) equation:

$$M_{1/2} \simeq \frac{4}{G} \sigma_{\nu}^2 R_e. \tag{1}$$

The R_e in this equation is defined as the 2D-projected half-light radius from elliptical fits, which is equivalent to our a_h . $M_{1/2}$ is the mass enclosed within this R_e .

The V-band luminosity was calculated by converting the integrated V-band magnitude using a solar $M_V = 4.83$. We divided the $M_{1/2}$ calculated above by the resulting L_V for the

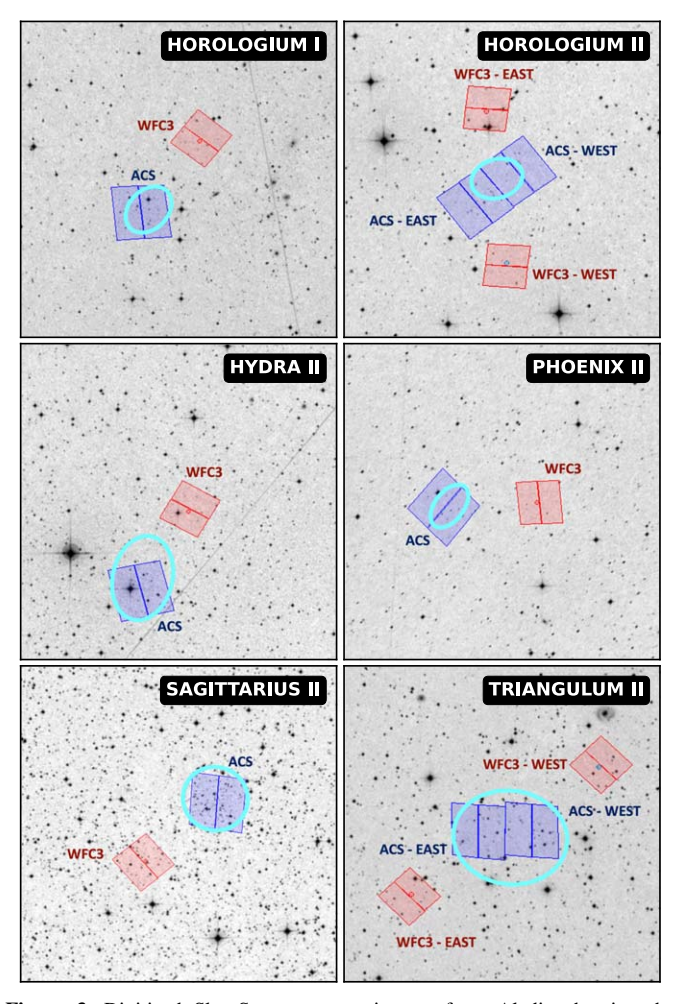


Figure 3. Digitized Sky Survey cutout images from Aladin showing the relative size of our measured half-light ellipses (a_h ; semimajor axis) and HST fields of view. North is up, and east is to the left for all panels. The ACS FOV in blue has a side length of 202"; the WFC3 FOV in red has a side length of 162". For targets with multiple ACS pointings, the corresponding WFC3 offfeld is labeled to match the ACS label, not the WFC3 relative physical positions. While our FOV/ a_h ratios are less than the Muñoz et al. (2012) recommendation (\sim 3), we are generally able to recover a_h values within 2σ agreement of past literature measurements.

mass-to-light ratio. Uncertainties reported in Table 2 are the 84th and 16th percentiles from the Monte Carlo simulation using the individual uncertainties on the mass and luminosity.

4. Results

4.1. Comparison of Measured Systems

Here, we report and compare our results to the literature for Hor I (Table 4), Hor II (Table 5), Hya II (Table 6), Phe II (Table 7), Sgr II (Table 8), and Tri II (Table 9). Figure 3 shows the relative sizes of our measured half-light radii against the observed fields of view. We have overplotted a cyan ellipse encompassing 50% of the surface density of each target (according to our best-fit exponential model) on a Digitized Sky Survey (DSS; Morrison 1995) optical cutout of the region of interest from Aladin (Bonnarel et al. 2000). Our ACS footprints are shown in blue, with the WFC3 off-fields in red.

We also discuss their classification status (e.g., star cluster or ultrafaint galaxy) and their possible association with the LMC. UFD candidates are typically confirmed to be galaxies based on velocity dispersion measurements determined spectroscopically (e.g., Simon & Geha 2007), as higher values suggest large mass-to-light ratios. The presence of a metallicity dispersion has also been used to support classification as a galaxy, as it suggests more than one period of star formation (Willman & Strader 2012). Particularly relevant here is the work of Fu et al. (2023), which estimated photometric metallicity distribution functions (MDF) and dispersion values for a few of the objects in our sample using narrowband HST imaging. Their analysis showed good agreement with smaller samples of spectroscopic measurements, and we include a discussion of their results for the applicable targets here.

Another classification technique that has recently been applied to UFDs relies on stellar mass segregation (Baumgardt et al. 2022). Energy equipartition should cause high-mass stars to become more centrally concentrated within a cluster, while the low-mass stars move farther out. The timescale for this process is longer in stellar systems that inhabit DM halos. As such, systems that show no sign of stellar mass segregation are more likely to be galaxies than star clusters. We report the Baumgardt et al. (2022) classification alongside or in lieu of the spectroscopic determination for completeness.

For brevity, we note that four of our targets (Hor I and Phe II discussed here; Ret II and Tuc II discussed in Section 4.2) were discovered concurrently by Koposov et al. (2015b) and Bechtol et al. (2015) using data from the first year of the Dark Energy Survey (DES). Koposov et al. (2015b) reported azimuthally averaged radii (r_h) rather than elliptical semimajor axis lengths (a_h) for their physical sizes.²² In our written comparisons, we present these r_h values but also include the physical a_h that we calculated using their ϵ values. The uncertainties reported on a_h in Tables 4, 7, 11, and 12 are from a Monte Carlo using the Koposov et al. (2015b) r_h , ϵ , and (m-M) values.

For all of the targets in our paper except for Hya II, Moskowitz & Walker (2020) reported "circularized" projected half-light radii²³ (our r_h) in arcminutes. To ease comparison, we converted the Moskowitz & Walker (2020) fit r_h to an a_h in arcminutes using their reported ϵ . We denote a_h values derived using the exponential model as $a_{h, \exp}$ and those from the Plummer model as $a_{h,p}$.

Figures 4 and 5 show the 1D surface density model profiles for the six UFDs that we measured, as well as the binned surface density values. Note that these 1D profiles were not fit to the binned data, but are rather the result of flattening the best-fit 2D model profiles. The x-axis is the elliptical radius, R_{ell} , which can be described as the radial distance when the major axis is aligned with the position angle (see Richstein et al. 2022, Equation (3) for the full mathematical expression). The left column shows only the measurements from this work, while the middle and right column compare our findings to past literature values for the exponential and Plummer models, respectively. We normalized the areas under the curve from the literature to our area values.

4.1.1. Horologium I

Both Koposov et al. (2015b) and Bechtol et al. (2015) were unable to constrain a position angle for Hor I, and Koposov

 $^{^{22}}$ We note that the $r_{\rm maj}$ values given in Koposov et al. (2015b) are the exponential scale lengths, $a_h/1.68$.

Moskowitz & Walker (2020) fit both a one- and three-component Plummer; we choose to report the best-fitting values from the one-component model as that model is most similar to the Plummer function that we adopted.

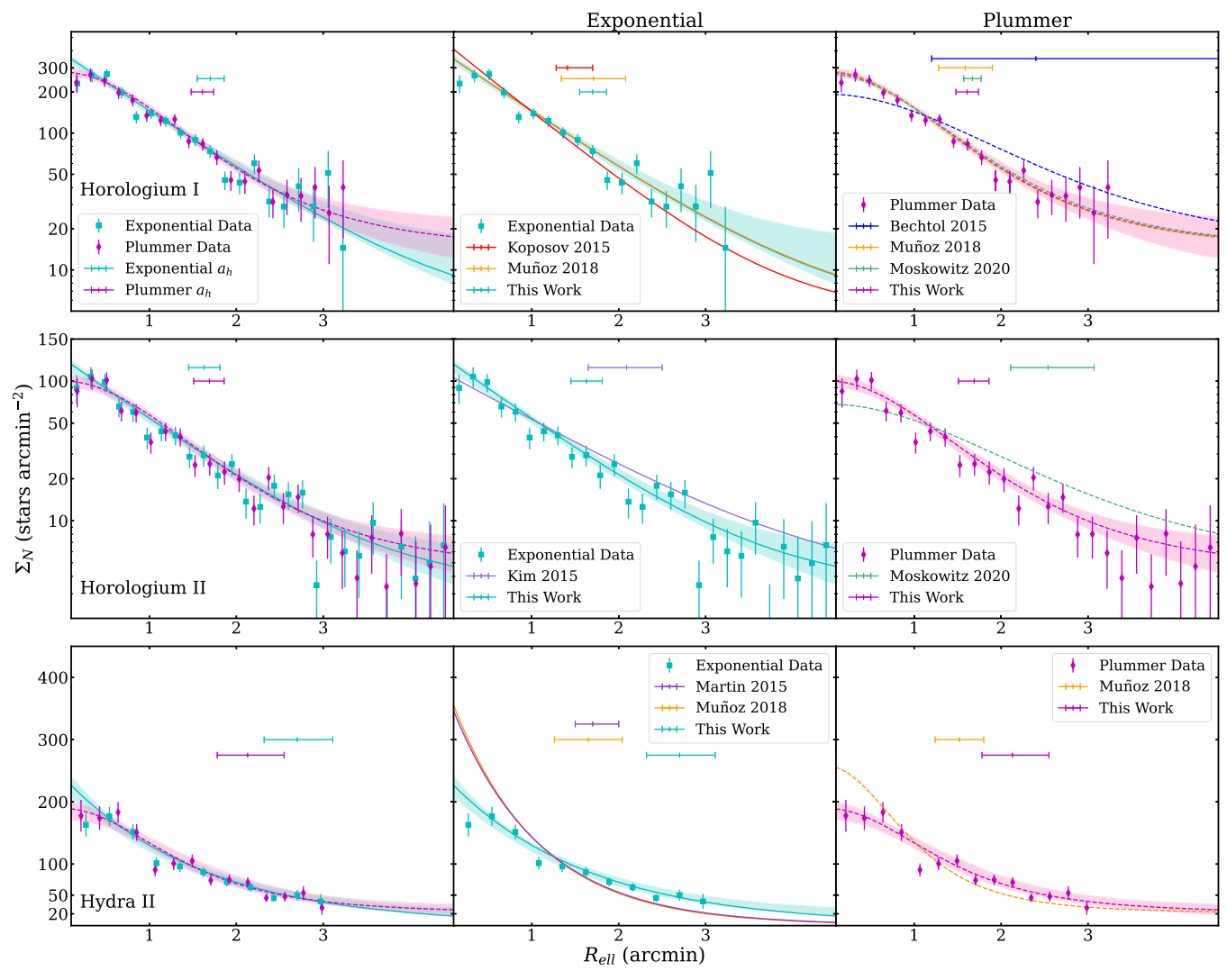


Figure 4. The 1D surface density profiles of Hor I (top row), Hor II (middle), and Hya II (bottom) plotted against the elliptical radius, R_{ell} . The left column shows the surface density measurements of the annularly binned data, at increments of $0.1a_h$ for the respective models (exponential, cyan; Plummer, magenta). Uncertainties are derived from Poisson statistics. The plotted curves represent the 1D profiles produced with the best-fit parameters of the 2D data. Floating horizontal lines represent the a_h measurements and their uncertainties. The middle column shows our exponential fits and 1D surface density measurements compared to existing literature measurements. The 1D profiles from literature fits are normalized to have an area under the curve equal to ours. The right column is the same as the middle, except for the Plummer model rather than the exponential. Note the agreement, despite the surface density profiles being fit to 2D-binned data rather than the 1D-binned data also shown here.

et al. (2015b) were only able to give an upper limit on its ellipticity using the discovery data. The two teams also reported different radii: Koposov et al. (2015b) estimated Hor I to have a \sim 1'.3 azimuthally averaged radius ($a_{h, \exp} \sim$ 1'.4), while Bechtol et al. (2015) reported a Plummer radius of \sim 2'.4 with large uncertainties. The next set of published structural parameters for Hor I was from Muñoz et al. (2018), who fit both Plummer and exponential models to photometry that they performed on the public DES data. Muñoz et al. (2018) measured an exponential half-light radius of \sim 1'.7, and a Plummer half-light radius of \sim 1'.6. The $a_{h,p}$ of Moskowitz & Walker (2020) was \sim 1'.7.

Walker (2020) was ~ 1.7 . Our $a_{h, \exp} = 1.70^{+0.16}_{-0.15}$ and $a_{h, p} = 1.61 \pm 0.13$ agree within 1σ with all past literature measurements. Using the previous Muñoz et al. (2018) $a_{h, \exp} = 1.71$ as a benchmark, the FOV/ a_h ratio would be just short of 2, although Hor I was one of the targets for which over 1000 sources were used in the structural fitting. Our θ and ϵ values for both the exponential and Plummer fits additionally agree within 1σ with the Muñoz et al. (2018). Our empirically derived $M_V = -3.4 \pm 0.2$ mag is also in agreement with past literature values.

Shortly after publishing the discovery paper, Koposov et al. (2015a) reported on follow-up data of Ret II and Hor I taken with the Very Large Telescope (VLT) FLAMES-GIRAFFE spectograph. For Hor I, they confirmed five member stars and found a kinematic dispersion of $4.9^{+2.8}_{-0.9}$ km s⁻¹, corresponding to a mass-to-light ratio of $\sim 570~M_{\odot}/L_{\odot}$. Although Koposov et al. (2015a) also measured a low metallicity dispersion (0.17 dex), they found that the low [Fe/H] = -2.76 and large mass-to-light ratio made it consistent with the other UFD galaxies known at the time.

A more detailed spectroscopic analysis based on three member stars using VLT FLAMES-UVES and the MIKE spectograph on the Magellan-Clay Telescope was published by Nagasawa et al. (2018). Their team found a similarly low average $[Fe/H] \sim -2.6$. The Baumgardt et al. (2022) mass-segregation measurement was not significant, supporting the

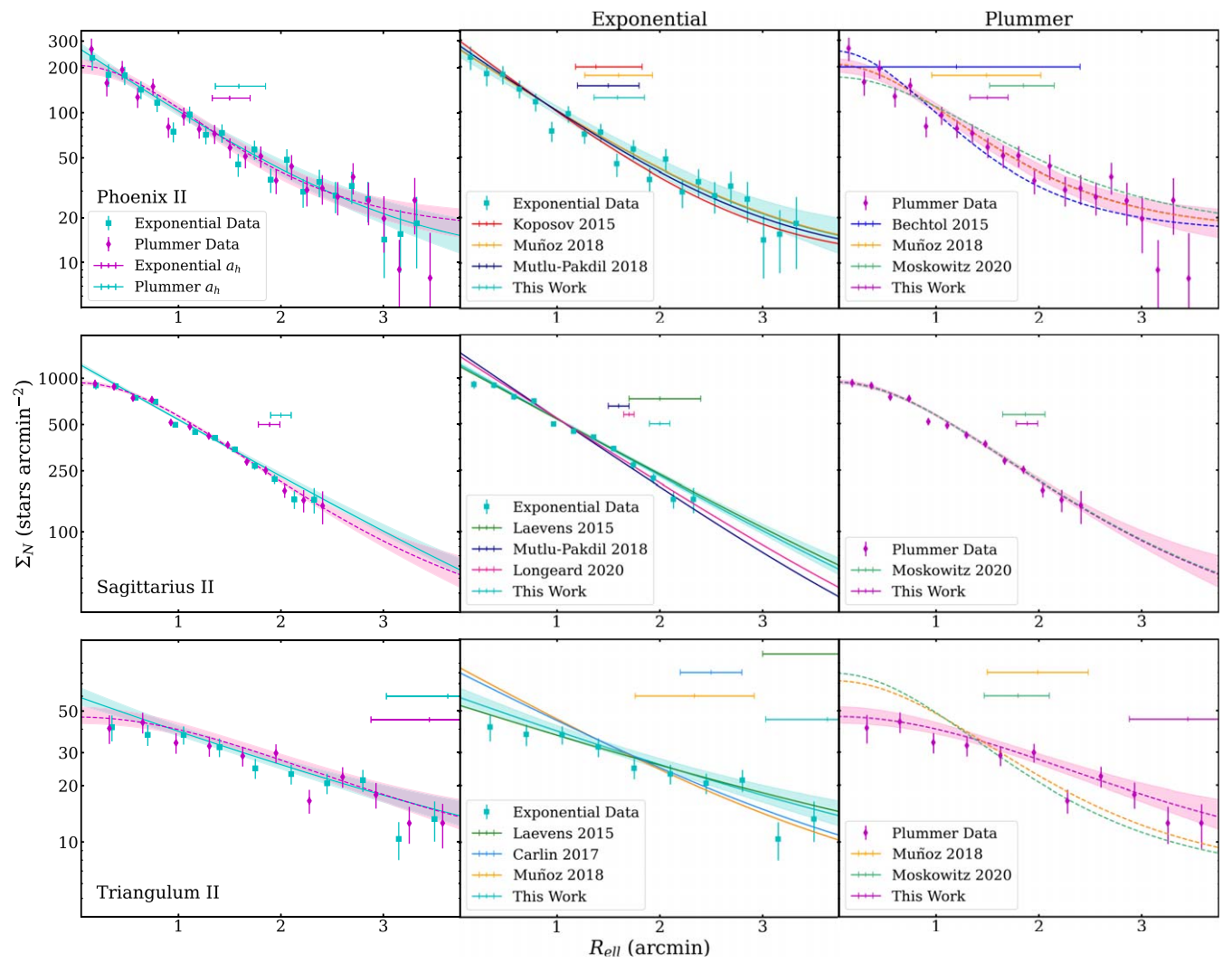


Figure 5. The same as Figure 4, for the targets Phe II (top row), Sgr II (middle), and Tri II (bottom).

classification of Hor I as a dwarf galaxy. From HST narrowband imaging of 27 stars, Fu et al. (2023) calculated an average [Fe/H] = $-2.79^{+0.12}_{-0.13}$ dex, and a $\sigma_{\rm [Fe/H]}=0.56^{+0.11}_{-0.09}$ dex. Removing a possible higher-metallicity outlier, the $\sigma_{\rm [Fe/H]}$ dropped to $0.41^{+0.11}_{-0.10}$ dex. Either metallicity spread is consistent with Hor I being a galaxy.

4.1.2. Horologium II

Kim & Jerjen (2015) discovered Hor II in the DES Y1A1 images, measuring an $a_{h, \exp} = 2!09^{+0.44}_{-0.41}$ (r_h in their paper). The only other structural parameter measurement is from Moskowitz & Walker (2020); using DES DR1, they fit $a_{h,p} \sim 2!5$, which agreed within 1σ . Hor II is one of our targets that had two telescope pointings, giving us a combined FOV of approximately $3!.3 \times 6!7$. The observations were oriented for maximal coverage along the semimajor axis, making our FOV/ a_h ratio (with the Kim & Jerjen 2015 value as a reference) slightly over 3 along that direction.

Our $a_{h, \rm exp}=1'.63\pm0.18$ measurement is just outside of being within 1σ agreement with the Kim & Jerjen (2015) value. Our $a_{h, \rm p}=1'.69^{+0.18}_{-0.17}$ is within 1.7σ of the Moskowitz & Walker (2020) value. Our exponential θ and ϵ values agree with the

Kim & Jerjen (2015) within 1.5σ and 1.6σ , respectively. For the Plummer model, our θ and ϵ are within 1σ and 1.1σ of the Moskowitz & Walker (2020) values. Our integrated $M_V = -2.1 \pm 0.2$ mag is 0.5 mag fainter than the $M_V = -2.6$ presented by Kim & Jerjen (2015), but still within 1.8σ agreement.

There has not yet been a spectroscopic study of Hor II, but Baumgardt et al. (2022) found no evidence for mass segregation and suggested that Hor II is likely a dwarf galaxy.

4.1.3. Hydra II

Martin et al. (2015) discovered Hya II serendipitously in data from the Survey of the Magellanic Stellar History (SMASH; Nidever et al. 2017), which used the Dark Energy Camera (DECam) on the Blanco 4 m telescope. They reported an $a_{h, \exp} = 1.7$ (r_h in their paper), with the caveat that the chip gaps and a bright foreground star near the center of the galaxy added uncertainty to the measurement. The Muñoz et al. (2018) measurement from the DECam data gave an $a_{h, \exp} \sim 1.7$ and an $a_{h, \exp} \sim 1.5$.

Our best-fit $a_{h,\exp}$ is $2'.70^{+0.41}_{-0.38}$, and our $a_{h,p}$ is $2'.13^{+0.42}_{-0.35}$, which are within 2σ and 1.4σ of the Muñoz et al. (2018) values,

respectively. Hya II is another target for which we have over 1000 sources; however, the saturated star mentioned in the Martin et al. (2015) discovery paper is also near the center of our frame. With the Muñoz et al. (2018) $a_{h, \exp} = 1!$ 65 as a reference, our FOV/ a_h is \sim 2. This discrepancy is thus likely due to the limited FOV, the position of the chip gap, and the saturated star. As this field was not optimized with structural measurements as a science goal, we consider the Muñoz et al. (2018) measurement based on a wider FOV to be more reliable.

From our fit, we measured a center approximately 45" from the original Martin et al. (2015) value. To investigate whether this was significant, or an artifact from our smaller FOV combined with the saturated star, we downloaded the SMASH DR2 object catalog (Nidever et al. 2021) for the appropriate region. We applied a distance cut to only consider sources within 6' of the Martin et al. (2015) center, as well as quality cuts for $|SHARP| \le 0.4$ and $\chi < 2$. Additionally, we required prob $\neq 0$, where prob is the average SExtractor (Bertin & Arnouts 1996) "stellaricity probability value." We ran our fitting code on the SMASH data and recovered a center that was $\sim 40''$ from the Martin et al. (2015) value, but within 1.4σ of our newly derived HST value. It is possible that the shallower nature of the discovery data led to a different stellar density center than is fit by the two more recent, deeper data sets. Our $M_V = -4.6^{+0.2}_{-0.3}$ mag is consistent with the previous measurements from Martin et al. (2015) and Muñoz et al. (2018).

Kirby et al. (2015b) presented Keck II/DEIMOS spectroscopy for 13 member stars of Hya II. They reported 90% and 95% confidence levels for the upper limits of the velocity dispersion corresponding to upper limits on the mass-to-light ratios of 200 and 315 M_{\odot}/L_{\odot} , respectively. Kirby et al. (2015b) were able to marginally resolve a metallicity dispersion of ~ 0.40 dex, and suggested that this supports tentative classification as a galaxy. This dispersion paired with the large physical radius more strongly supports the dwarf galaxy nature of Hya II, although Simon (2019) does not list Hya II among the spectroscopically confirmed UFDs. More recently, Fu et al. (2023) measured the MDF of Hya II from HST imaging and reported an average [Fe/H] of $-3.08^{+0.11}_{-0.12}$ dex, and a $\sigma_{\rm [Fe/H]} = 0.33^{+0.12}_{-0.13}$ dex based on 30 stars. Including a more metal-rich possible outlier, the $\sigma_{\rm IFe/HI}$ increased to $0.47^{+0.13}_{-0.12}$ dex.

4.1.4. Phoenix II

From the DES data for Phe II, Koposov et al. (2015b) reported an azimuthally averaged r_h of 1/3 ($a_{h, \exp} \sim 1$ /7), and Bechtol et al. (2015) published an $a_{h,p}$ value of \sim 1/2, although Bechtol et al. (2015) were unable to constrain a position angle or ellipticity. Using the same DES data, Muñoz et al. (2018) measured similar values, with $a_{h, \exp} \sim 1$ /6 and $a_{h,p} \sim 1$ /5. Mutlu-Pakdil et al. (2018) took follow-up data with Megacam at the Magellan Clay telescope, reaching \sim 2–3 mag deeper, and reported an exponential $a_{h, \exp} \sim 1$ /5. The most recent literature measurement from Moskowitz & Walker (2020) used DES DR1 and fit $a_{h,p} \sim 1$ /9.

Our $a_{h,\text{exp}} = 1.58^{+0.26}_{-0.23}$ is consistent with the three past literature measurements. Our $a_{h,\text{p}} = 1.5^{+0.20}_{-0.17}$ is also consistent with the past Plummer profile fits. Broadly, our θ and ϵ values are consistent with past measurements, with the exception of Moskowitz & Walker (2020). Using the Muñoz et al. (2018)

 $a_{h, \rm exp} = 1.60$, our FOV/ a_h is 2.1. We calculate $M_V = -2.9^{+0.2}_{-0.1}$ mag, consistent with all past literature measurements.

VLT/FLAMES spectroscopy for Phe II was presented in Fritz et al. (2019), who measured a velocity dispersion of $11.0 \pm 9.4 \text{ km s}^{-1}$ and an intrinsic metallicity spread of 0.33 dex for the five stars that the authors identified as members. Their assessment of Phe II as a galaxy agreed with the previous suggestion by Mutlu-Pakdil et al. (2018), who based their classification on its ellipticity and position in the size–luminosity plane. Baumgardt et al. (2022) found no significant mass segregation, supporting the dwarf galaxy classification; they noted, however, that, because of its large relaxation time, there is still the possibility that Phe II could be a star cluster. Fu et al. (2023) report a mean $[Fe/H] = -2.36^{+0.18}_{-0.16}$ dex, and a $\sigma_{[Fe/H]} = 0.41^{+0.22}_{-0.17}$ dex from 10 HST stars, and paired with the mass segregation information, supported the classification of Phe II as a galaxy.

4.1.5. Sagittarius II

Laevens et al. (2015a) reported the discovery of this satellite from the Panoramic Survey Telescope and Rapid Response System (Pan-STARRS 1, PS1; Chambers et al. 2016) survey data, and measured $a_{h,\rm exp} \sim 2'$ (r_h in their paper). This satellite's nature (cluster versus galaxy) was ambiguous at the time of discovery leading to the dual name of Sagittarius II/Laevens 5; however, all subsequent papers adopted the Sgr II naming. Mutlu-Pakdil et al. (2018) presented deeper Magellan Megacam imaging with an $a_{h,\rm exp}$ of $\sim 1'.6$, which agreed within the uncertainties with that of Laevens et al. (2015a). Longeard et al. (2020) took deep observations with the Canada–France–Hawaii Telescope (CFHT) MegaCam and presented $a_{h,\rm exp} \sim 1'.7$ (r_h in their paper). Moskowitz & Walker (2020) used Pan-STARRS DR1 (Chambers et al. 2016) and fit a larger $a_{h,p} \sim 1'.9$.

Our $a_{h,\text{exp}} = 1.94 \pm 0.08$ is larger than recent measurements, although consistent with Laevens et al. (2015b). We differ at a level of $\sim 2.6\sigma$ with Longeard et al. (2020) and Mutlu-Pakdil et al. (2018). Based on the Longeard et al. (2020) $a_{h,\text{exp}} = 1.7$, our FOV/ a_h is a little under 2. Similarly to Mutlu-Pakdil et al. (2018) and Longeard et al. (2020), we also find very little ellipticity, with $\epsilon < 0.03$ and < 0.09 at the 95% confidence level. Additionally, our $a_{h,p} = 1.85^{+0.07}_{-0.08}$ is consistent with the measurement of Moskowitz & Walker (2020).

Reported position angle values vary widely, which could be related to the low ellipticity and therefore the lack of a clear semimajor axis. Our measured θ values agree within 0.1σ and 0.6σ to the Longeard et al. (2020) and Moskowitz & Walker (2020) values, respectively; however, our $\epsilon < 0.09$ suggests that θ may not be meaningful here. Our $M_V = -5.3 \pm 0.2$ mag is consistent with those from Laevens et al. (2015b) and Longeard et al. (2020), but not with the Mutlu-Pakdil et al. (2018) $M_V = -4.2 \pm 0.1$ mag.

Simon et al. (2019) presented a spectroscopic study of Sgr II based on Magellan/IMACS data, reporting a velocity dispersion of 1.6 ± 0.3 km s⁻¹ and a metallicity dispersion <0.08 dex at the 95% confidence limit, suggesting that Sgr II could be a globular cluster. From Keck II/DEIMOS data, Longeard et al. (2020) measured a velocity dispersion of $2.7^{+1.3}_{-1.0}$ km s⁻¹ and a combined photometric and spectroscopic metallicity dispersion of $0.12^{+0.03}_{-0.02}$ dex. Longeard et al. (2021) used new VLT/FLAMES data combined with the DEIMOS spectra, measuring a smaller velocity dispersion of 1.7 ± 0.5 km s⁻¹ from 113 stars.

From 15 stars, they calculated an unresolved metallicity dispersion less than 0.20 dex at the 95% confidence limit. Longeard et al. (2021) thus concluded that Sgr II is a globular cluster. Baumgardt et al. (2022) additionally found a high level of mass segregation, supporting the star cluster classification. While Fu et al. (2023) do not present their analysis on Sgr II, they state that their results are consistent with the globular cluster status.

4.1.6. Triangulum II

This was the first discovered ultrafaint satellite from the PS1 data by Laevens et al. (2015b), who then took follow-up imaging with the Large Binocular Cameras at the Large Binocular Telescope. Unable to determine whether this satellite was a cluster or dwarf galaxy, Laevens et al. (2015b) gave it the double name of Laevens 2 and Triangulum II. The initial $a_{h, \rm exp}$ value from Laevens et al. (2015a; reported as r_h) was 3'.9, although they included the caveat that, with the low contrast of the stellar overdensity to the background, deeper data would provide a stronger measurement.

Carlin et al. (2017) presented further follow-up deep imaging from the Subaru Hyper Suprime-Cam that reached \sim 2 mag deeper than the discovery data and increased the overdensity-to-background contrast. They derived an $a_{h, \rm exp}$ of 2'.5, consistent within 1.5 σ to the Laevens et al. (2015a) value. Muñoz et al. (2018) derived a similar exponential $a_{h, \rm exp} \sim 2'$.3 and a slightly smaller $a_{h, \rm p} \sim 2'$ using Pan-STARRS data from the discovery team. Moskowitz & Walker (2020) measured an $a_{h, \rm p} \sim 1'$.8 from the Pan-STARRS data.

Tri II had two ACS pointings, giving us an FOV of $\sim 3.3 \times 6.7$, and a maximum possible FOV/ a_h value of ~ 2.9 along the semimajor axis. We measured $a_{h, \rm exp} = 3.50^{+0.59}_{-0.65}$, larger, but within 1.4σ agreement with Carlin et al. (2017) and Muñoz et al. (2018); our value is smaller than the Laevens et al. (2015b) measurement, although consistent within 0.4σ . Our $a_{h,p} = 3.25^{+0.51}_{-0.59}$ measurement is larger but within 1.7σ agreement with the Muñoz et al. (2018) Plummer measurement and 2.2σ agreement with the Moskowitz & Walker (2020) value.

Our θ and ϵ values are consistent with both the Carlin et al. (2017) and Moskowitz & Walker (2020) measurements. The θ and ϵ values from our exponential models are within 1.3σ and 1.6σ of the Muñoz et al. (2018); for the Plummer model, they are within 0.9σ and 0.6σ , respectively. Our fits are most consistent with the larger a_h and smaller ellipticity presented in the Laevens et al. (2015a) discovery paper. The low number of stars in this galaxy and the slight gap between the two ACS pointings may have affected our fits, and we advise adopting either the Carlin et al. (2017) or Muñoz et al. (2018) values. The integrated $M_V = -1.3 \pm 0.2$ mag that we measure is in 1σ agreement with the three past literature determinations.

Numerous spectroscopic studies of Tri II have been published (Kirby et al. 2015a, 2017; Martin et al. 2016; Venn et al. 2017; Ji et al. 2019), often with results hinting at a dwarf galaxy nature, but with no definitive conclusions. The most recent spectroscopic study by Buttry et al. (2022) combined new MMT/Hechtochelle data with the existing Keck II/DEIMOS set and presented an upper limit on the velocity dispersion of 3.4 km s⁻¹ at the 95% confidence level. Additionally, with new Gaia PM information confirming two questionable member stars used in the Kirby et al. (2017) metallicity dispersion measurement, Buttry et al. (2022) used

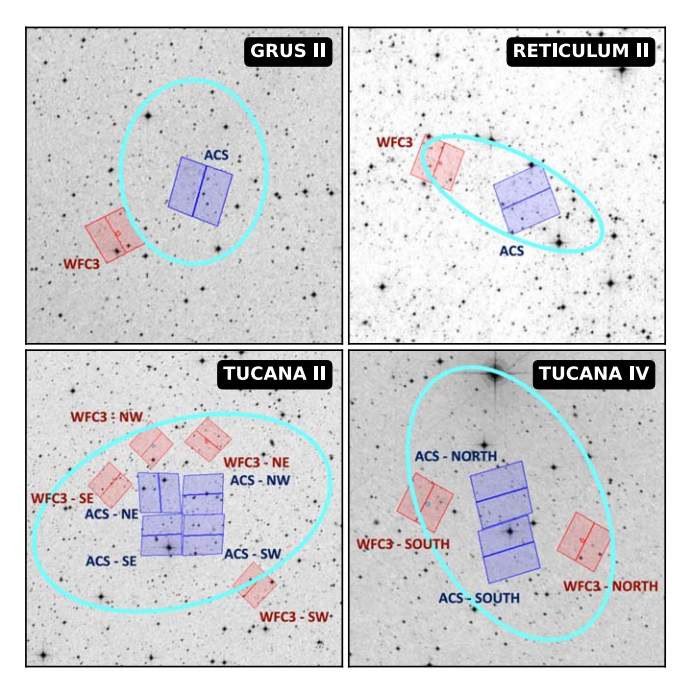


Figure 6. Similar to Figure 3, for the four targets that we present photometry for but do not measure structural parameters. North is up, and east is to the left in all panels. The ACS FOV in blue has a side length of 202"; the WFC3 FOV in red has a side length of 162". For targets with multiple ACS pointings, the corresponding WFC3 off-field is labeled to match the ACS label, not the WFC3 relative physical positions.

their combined data to report a value of $0.46^{+0.37}_{-0.09}$ dex; this large spread lends stronger support to a Tri II galaxy classification. Additionally, the Baumgardt et al. (2022) study found no mass segregation and supported this conclusion.

4.2. Review of Nonmeasured Systems

For Gru II (Table 10), Ret II (Table 11), Tuc II (Table 12), and Tuc IV (Table 13), we give a brief review of past morphological studies. Figure 6 shows the coverage of our HST observations relative to past literature measurements of the target half-light ellipses.

4.2.1. Grus II

Gru II was the ultrafaint candidate with the highest σ detection discovered in the second year of DES data, and had no significant ellipticity or asphericity (Drlica-Wagner et al. 2015). As such, there would not be a corresponding a_h ; Drlica-Wagner et al. (2015) reported $r_h = 6'$. Using the DES Y3A2 catalog, ²⁴ Simon et al. (2020) repeated the structural analysis and recovered an $a_{h,p}$ (referred to as $r_{1/2}$) of 5! 9 and an upper limit on the ellipticity of 0.21. The Moskowitz & Walker (2020) $a_{h,p}$ measurement from DES DR1 (Abbott et al. 2018) data was larger, at ~7! 8, yet within 1.7 σ and 2.5 σ of the Drlica-Wagner et al. (2015) and Simon et al. (2020) values, respectively.

We did not fit structural parameters for Gru II, as past measurements of its size have found $a_h \sim 6'$ (Drlica-Wagner et al. 2015; Moskowitz & Walker 2020; Simon et al. 2020), and our single ACS pointing only extends to $\sim 0.25 a_h$, which is insufficient for a robust morphology measurement.

 $^{^{24}}$ DES Y3A2 refers to an internal DES release. The public DES DR1 was based on this (Abbott et al. 2018).

The first spectroscopic observation of Gru II was performed by Simon et al. (2020), who identified 21 member stars with Magellan/IMACS spectroscopy. They were unable to clearly resolve a velocity dispersion, but did report 90% and 95.5% upper limits. Additionally, Simon et al. (2020) did not detect a metallicity spread; however, based on the low metallicity ([Fe/H] = -2.51 ± 0.11 dex) and large size, they concluded Gru II is likely a dwarf galaxy. Using DOLPHOT photometry of HST data, Baumgardt et al. (2022) did not find significant mass segregation among the member stars, leading them to also conclude that Gru II is likely a dwarf galaxy.

4.2.2. Reticulum II

From the DES data, in their discovery papers, Koposov et al. (2015b) measured an r_h of $\sim 3'.6$ ($a_{h, \rm exp} \sim 5'.7$), and Bechtol et al. (2015) measured an $a_{h, \rm p} \sim 6'$. Muñoz et al. (2018) fit slightly smaller values of $a_{h, \rm exp} \sim 5'.4$ and $a_{h, \rm p} \sim 5'.5$ to the same DES data. Mutlu-Pakdil et al. (2018) used deeper (by $\sim 2-3$ mag) data from Megacam to fit an $a_{h, \rm exp} \sim 6'.3$, in agreement with the original Bechtol et al. (2015) measurement. The Moskowitz & Walker (2020) $a_{h, \rm p}$ from DES DR1 was slightly larger, at $\sim 6'.6$. We did not fit structural parameters for Ret II, as the ACS FOV covers approximately $0.25a_h$.

Three independent spectroscopic studies of Ret II were published in the months following the discovery papers (Koposov et al. 2015a; Simon et al. 2015; Walker et al. 2015), all concluding that Ret II had the kinematic and spectroscopic properties consistent with being a dwarf galaxy. Simon et al. (2015) presented Magellan/M2FS, VLT/GIRAFFE, and Gemini South/GMOS spectroscopy; from 25 member stars, they calculated a velocity dispersion of $3.3 \pm 0.7 \text{ km s}^{-1}$ and a metallicity dispersion of $0.28 \pm 0.09 \text{ dex}$. Walker et al. (2015) confirmed 17 member stars and reported a velocity dispersion of $3.6^{+1.0}_{-0.7} \text{ km s}^{-1}$ and a metallicity dispersion of $0.49^{+0.19}_{-0.14} \text{ dex using Magellan/M2FS data. Lastly, Koposov et al. (2015a) measured a velocity dispersion of <math>3.22^{+1.64}_{-0.49} \text{ km s}^{-1}$ and a metallicity dispersion of $0.29^{+0.13}_{-0.05} \text{ dex}$ from the VLT/GIRAFFE data.

The most recent spectroscopic study by Ji et al. (2023) updated these values to be $2.97^{+0.43}_{-0.35}$ km s⁻¹ and $0.32^{+0.10}_{-0.07}$ dex for the velocity and metallicity dispersion, respectively. Baumgardt et al. (2022) applied their mass-segregation method to Ret II and found results in agreement with the previous studies; however, they noted that due to the large relaxation time, the mass-segregation method alone would not be able to clearly determine the classification. Fu et al. (2023) used HST photometric metallicities from 76 stars to derive an average $[Fe/H] = -2.64^{+0.10}_{-0.11}$ dex, and $\sigma_{[Fe/H]} = 0.72^{+0.09}_{-0.08}$ dex. This large metallicity dispersion would strongly support a galaxy classification. They noted the large discrepancy with past spectroscopic studies and invited follow-up observations for better membership determination.

4.2.3. Tucana II

The discovery parameters for Tuc II from Koposov et al. (2015b) and Bechtol et al. (2015) were quite different, with the former reporting an azimuthally averaged r_h of 9.8 ($a_{h, \exp} \sim 12.9$) and the latter publishing an $a_{h, p}$ of 7.2. This discrepancy could be due in part to different CMD masking techniques for member selection. While Bechtol et al. (2015) noted that there was some elongation in the outer regions of the

detected overdensity, they suggested that the distortion was likely noise related and showed that, after their CMD-masking, the overdensity is much rounder. Figure 12 of Koposov et al. (2015b) shows the CMD-masked stars in the Tuc II field with the elongation still visible. Moskowitz & Walker (2020) fit DES data for Tuc II and recovered $a_{h,p} \sim 13'.5$, consistent with the $a_{h,exp}$ of Koposov et al. (2015b) within 1σ .

Our FOV included four ACS pointings, for a maximum field-width of less than 7'. We did not fit the structural parameters as, although literature a_h measurements varied from \sim 7' to 13'.5, our FOV would cover at most the inner one-half of the galaxy.

Using eight probable member stars with spectroscopy from the Michigan/Magellan Fiber System (M2FS), Walker et al. (2016) measured a velocity dispersion for Tuc II of $8.6^{+4.4}_{-2.7}~{\rm km~s^{-1}}$ and a metallicity dispersion of $0.23^{+0.18}_{-0.13}$ dex and concluded that it is a dwarf galaxy. The velocity dispersion has since been remeasured by Chiti et al. (2023), who used 16 member stars and calculated a value of $3.8^{+1.1}_{-0.7}~{\rm km~s^{-1}}$.

4.2.4. Tucana IV

Tuc IV had the largest angular size of the ultrafaint satellite candidates discovered in the DES year 2 data, with an azimuthally averaged $r_{\rm h}=9.1$ ($a_{h,\rm p}\sim11.8$; Drlica-Wagner et al. 2015). The analysis using DES DR1 by Moskowitz & Walker (2020) measured a slightly smaller $a_{h,\rm p}\sim9.2$, consistent within 1.3σ with the Drlica-Wagner et al. (2015) value. From the DES Y3A2 catalog, Simon et al. (2020) published the most recent structural parameters for Tuc IV, reporting $a_{h,\rm p}\sim9.3$. Our two ACS pointings would cover approximately the inner one-third of the target, so we did not attempt to characterize the morphology with our HST data.

Simon et al. (2020) published the first spectroscopic study of Tuc IV, significantly resolving a velocity dispersion of $4.3^{+1.7}_{-1.0}$ km s⁻¹. From eight RGB stars, they measured a metallicity dispersion of $0.18^{+0.20}_{-0.18}$ dex. Simon et al. (2020) calculated a mass-to-light ratio of $3100^{+2900}_{-1600} M_{\odot}/L_{\odot}$, indicating a DM dominated nature, and thus spectroscopically confirmed Tuc IV as a galaxy.

5. Discussion

5.1. Uses for HST Imaging in Structural Analysis

The HST MW UFD Treasury Program (GO-14734) contains a wealth of data, and precision photometry is essential for optimizing its value. Here, we have presented a subset of the data and an example use case, with a focus on targets that have been kinematically linked to the LMC. While a space telescope with a small FOV would not be the premier choice for morphological studies, these types of analyses are still beneficial as ancillary uses for the data. The depth and resolution of the images have given us the ability to characterize the inner surface densities, and in some cases, recover a full set of structural parameters in agreement with past literature. Five out of 12 structural fits (six targets, two models) for a_h fall within 1σ of previously measured values, and all fall within 3σ even though we do not meet the suggested FOV and number of sources criteria (e.g., Muñoz et al. 2012).

One of the advantages of high-resolution, space-based imaging is the ability to more clearly distinguish stars from galaxies, as the PSFs are not affected by the atmosphere. This

can be important for determining whether apparent structural overdensities from ground-based observations are meaningful or if they are from contaminating background sources.

An illustrative example of this is when the analysis of ground-based, Megacam imaging of Leo V seemed to suggest the existence of a debris stream (Sand et al. 2012), and follow-up space-based observations showed otherwise. Mutlu-Pakdil et al. (2019) presented HST/ACS imaging centered on the overdensity in the Leo V field, and showed that almost half of the photometric sources were background galaxies. The higher-precision photometry also revealed that many of the true stars from the overdensity were unlikely to be Leo V members.

In the case of Hercules, however, photometry of off-center HST/ACS fields contained a main sequence consistent with the stellar population identified in the central pointing, supporting the existence of Hercules' elongation (Mutlu-Pakdil et al. 2020). The Mutlu-Pakdil et al. (2019, 2020) studies both relied on archival imaging of the central regions of their target UFDs, much like the observations we have presented here. Their results highlight how we should be cautious in our interpretations of apparent low surface-brightness features, yet at the same time, how important follow-up, space-based imaging is in order to gain more insight into what the structure of a satellite can tell us.

5.2. The Importance of UFD Structural Characterization

As UFDs are thought to reside in the least massive DM halos observed to be hosting galaxies (e.g., Bullock & Boylan-Kolchin 2017; Simon 2019), their mass accretion histories and their sensitivity to tidal forces have implications for their role in hierarchical structure formation (e.g., Mutlu-Pakdil et al. 2020). While we cannot observe directly how UFDs have evolved to their present state, their morphologies may still reflect major events that disturbed their original mass distributions. For example, early morphology studies noted that UFDs were more elliptical than classical dwarfs, with a possible explanation being that these less massive galaxies were more susceptible to tidal effects from the MW (e.g., Martin et al. 2008). While updated measurements from a larger sample size showed that there is little evidence to support a difference between the two populations in this respect (Sand et al. 2012; Simon 2019), the existence of UFD "tidal features" (and the need for a physical explanation) remains (e.g., Simon & Geha 2007; Sand et al. 2009; Muñoz et al. 2018; Mutlu-Pakdil et al. 2020).

One particularly interesting case is that of Tuc II, one of our limited-FOV targets with only photometry presented. Chiti et al. (2021) reported the discovery of member stars out to \sim 9 times the Bechtol et al. (2015) a_h and noted that the orbital parameters of Tuc II made tidal disruption an incompatible explanation. Soon after, simulation groups were able to reproduce UFD "tidal features" without invoking tidal heating from a more massive host galaxy (Tarumi et al. 2021; Goater et al. 2024). For example, assembly from less massive "building block galaxies" (Tarumi et al. 2021) as well as late-time dry accretion (Goater et al. 2024) can produce extended stellar halos and more elliptical stellar distributions. There has also been more interest in the stellar halos of dwarf galaxies, including how they could be built up through dwarfdwarf mergers (Deason et al. 2022) and how to systematically search for them observationally (e.g., Filion & Wyse 2021; Jensen et al. 2024; Longeard et al. 2023).

Tidal interactions with the MW are also a strongly supported mechanism for the formation of stellar halos around dwarf galaxies. Classical dwarfs, such as Fornax, Sculptor, and Ursa Minor I, have had member stars found at large radii, which dynamical models are able to explain by invoking the effects of Galactic tides, whether the target is on first infall (e.g., Fornax; Yang et al. 2022), was recently at pericenter (e.g., Sculptor, Sestito et al. 2023a), or has had multiple orbits around the MW (e.g., Ursa Minor I, Sestito et al. 2023b). Member stars at large galactocentric distances have also been studied in other UFDs, including Boötes I, Coma Berenices, Hercules, and Ursa Major I (Longeard et al. 2023; Waller et al. 2023; Ou et al. 2024). Both Galactic tidal effects (Filion & Wyse 2021; Longeard et al. 2022) and a minor merger (Waller et al. 2023) have been proposed as mechanisms for the extended structure in the case of Boötes I, while bursty feedback from star formation has been suggested for Coma Berenices and Ursa Major I (Waller et al. 2023).

5.3. LMC versus Non-LMC UFDs in the $M_V - r_h$ Plane

Sacchi et al. (2021) found tantalizing hints of differences between the SFHs of the LMC- versus non-LMC-associated UFDs, which inspired us to investigate whether the two UFD subgroups showed differences in other observational planes. One could postulate that environmental effects from the density differences in the early Universe, or more recently the MW halo, could have affected the two groups of satellites differently, perhaps leading to either more compact or extended morphologies based on length of time in the MW halo and pericenter distance.

To explore whether there were any differences between the two subgroups apparent in the M_V-r_h parameter space, we fit a line for each set of UFDs to broadly characterize the relationship. To account for the large uncertainty spaces, we drew M_V and r_h values for each galaxy in the two sets (LMC and non-LMC) using the reported values as the Gaussian mean and the reported uncertainties as the Gaussian σ . Additionally, we assume an intrinsic scatter in M_V at fixed r_h . This is modeled using a Gaussian with a σ set to the rms scatter of the data around the best-fit line, with a separately drawn value added to each M_V . For each set of redrawn values, we fit a linear regression model. We performed this procedure 10,000 times per set and show the median M_V value of the evaluated linear functions for r_h from 0 to 200 pc in Figure 7 (gold and dark blue solid lines for the LMC and non-LMC UFDs, respectively). The gold and dark blue shaded regions encompass the 16th to 84th percentiles of M_V values evaluated across the r_h space.

While the median trend lines overlap at magnitudes fainter than -3.5, at brighter magnitudes, they begin to diverge. This seems to agree with the Erkal & Belokurov (2020) finding that, at fixed luminosity, likely LMC satellites have slightly smaller r_h than MW satellites, which they postulated could be due to different tidal environments. To test the significance of this comparison, we ran a Monte Carlo that drew 10,000 sets of six random non-LMC associated UFDs with M_V and r_h values drawn using the previously described Gaussian technique. We fit a linear regression to each set of six galaxies and overplotted the region that encompasses the 16th to 84th percentiles in light blue on Figure 7. This region overlaps the LMC satellite trend line heavily and encompasses the space around five out of the

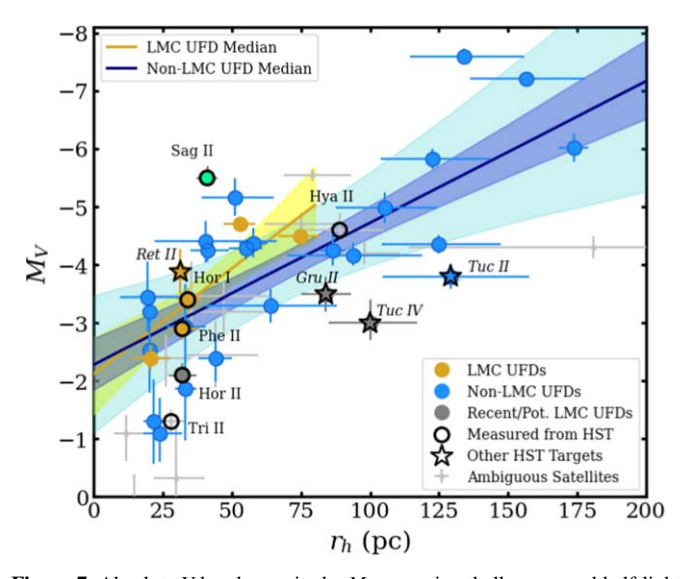


Figure 7. Absolute V-band magnitude, M_V , vs. azimuthally averaged half-light radius, r_h , for UFDs, UFD candidates, and the globular cluster Sag II (green circle). Golden markers represent the six LMC-associated UFDs, while the blue circles are the non-LMC confirmed UFDs. The three dark gray markers (one circle, two stars) represent the UFDs that are either thought to be recently captured or formerly associated with the LMC, which were not used in the trendline fits. Circles with bold black outlines (with labels) show measurements from this work. Star symbols are targets (with italicized labels) for which we present photometry, but do not fit structural parameters. Silver markers with errorbars are nonconfirmed UFDs, which were not used in the trendline fits. The solid gold (dark blue) line represents the median value from the Monte Carlo simulations for the LMC (non-LMC) UFD $M_V = r_h$ relation. The gold and dark dark blue shaded regions cover the 16th to 84th percentiles from the Monte Carlos for the respective sets. The cyan shaded region represents the 16th to 84th percentiles of lines fit to the six galaxy, non-LMC Monte Carlo simulation as described in Section 5.3. The light green band is where the yellow and cyan regions overlap, and the darkest shaded region is where all three uncertainty spaces overlap. Although the fit trend lines diverge, the overlapping uncertainty bands suggest no statistical difference.

six LMC UFDs, suggesting that the divergence of the median M_V - r_h relation is not statistically significant.

5.4. Observed and Simulated UFDs in the M_V-r_h Plane

Baryonic simulations have advanced to the extent that some are now able to resolve galaxy formation in the ultrafaint regime. We present a subset of these simulated UFD-analogs plotted in M_V versus r_h in Figure 8 along with observed UFDs, UFD candidates, and star clusters.

As simulation groups often report stellar mass (M_{\star}) and 3D, half-mass radii rather than M_V and 2D, projected half-light radii, respectively, some literature values had to be converted. When M_V and 2D r_h values were provided from the simulations, we plotted those. Otherwise, to place the simulated galaxies in a plane where the quantities are more readily comparable, we converted M_{\star} to M_V using a stellar-mass-to-light ratio of 2, which is reasonable for an ancient stellar population (e.g., Martin et al. 2008; Simon 2019). To convert the 3D radius values, we used the relation presented in Wolf et al. (2010):

$$R_e \simeq \frac{3}{4} r_{1/2},\tag{2}$$

where R_e is the 2D, projected half-light radius, and $r_{1/2}$ is the 3D, deprojected half-light radius. Assuming that all simulated galaxies have roughly spherical mass distributions, R_e is then

equivalent to r_h . The simulated galaxies are colored according to the reported baryonic mass resolutions, except for the points that come from The Next Generation Illustris (IllustrisTNG) formation model, as these were much lower resolution with star particle masses $\sim 10^4 M_{\odot}$. We will refer to these galaxies as being from the "TNG" model, which we introduce and discuss further below. Most of the simulations followed the CDM model, but there are some that used warm dark matter (WDM; e.g., Hogan & Dalcanton 2000; Barkana et al. 2001; Bode et al. 2001; Sommer-Larsen & Dolgov 2001) and self-interacting dark matter (SIDM; e.g., Davé et al. 2001; Rocha et al. 2013; Tulin & Yu 2018); these are shown with open markers. Basic properties of the simulations used are listed in Table 3.

For the data, we convert a_h values from the literature to r_h using the reported ϵ values. Plotted error bars are generated from a Monte Carlo using both the uncertainties on the a_h and ϵ values. To simplify the plot, we do not show error bars on the globular cluster values from the literature. Star clusters are classified here as "ultrafaint" if they have $M_V \geqslant -3$ (e.g., Cerny et al. 2023b). Literature values for classical dwarfs, UFDs, and ambiguous satellites are shown in black. For the purposes of this plot, we are not highlighting our new measurements but have included an extra square frame around the LMC-associated sample.

We have also included simulated galaxies from LYRA (Gutcke et al. 2022) even though no UFDs are produced, as this model created classical dwarf analogs similar to those from the other simulations considered. The LYRA set also has the highest resolution, with a baryonic particle mass of $4 M_{\odot}$ and is likely going to produce UFD analogs in future studies.

We also note that the TNG galaxies (Rose et al. 2023; J. Rose et al. 2024, in preparation) may not be considered direct UFD analogs due to limitations from their use of a pressurized equation of state. These galaxy formation prescriptions are identical to those used in IllustrisTNG (e.g., Pillepich et al. 2018), a well-known, large volume cosmological simulation that has been shown to be consistent with observed size relations for galaxies with $M_{\star} \gtrsim 10^9 M_{\odot}$ and to have good numerical convergence (Genel et al. 2018). While the TNG galaxies have much lower resolution than the other simulations, we include them because they offer a comparison between samples from both CDM and alternative DM models with the same baryonic physics. The ETHOS alternative DM models (Vogelsberger et al. 2016) included contain both suppression to the initial matter power spectrum in the form of dark acoustic oscillations, and SIDM with a self-consistently chosen velocity-dependent cross section. As the TNG ETHOS galaxies include more than the standard SIDM (which would use the CDM initial matter power spectrum), we will refer to them as ETHOS/SIDM.

5.4.1. Do Simulated UFDs Match Observations?

While there are many different metrics for determining how well simulations are producing UFDs (e.g., velocity dispersion, MDF), here, we choose to examine agreement in the M_V – r_h plane. From Figure 8, it can be seen that the Jeon et al. (2021a, 2021b) simulations (higher resolution, magenta x's) produce the highest number of UFD analogs that overlap with observed MW UFDs. EDGE (Agertz et al. 2020; Prgomet et al. 2022), FIRE-2 (Jahn et al. 2022; Wetzel et al. 2023) using both CDM and WDM (Bozek et al. 2019), GEAR (Revaz & Jablonka

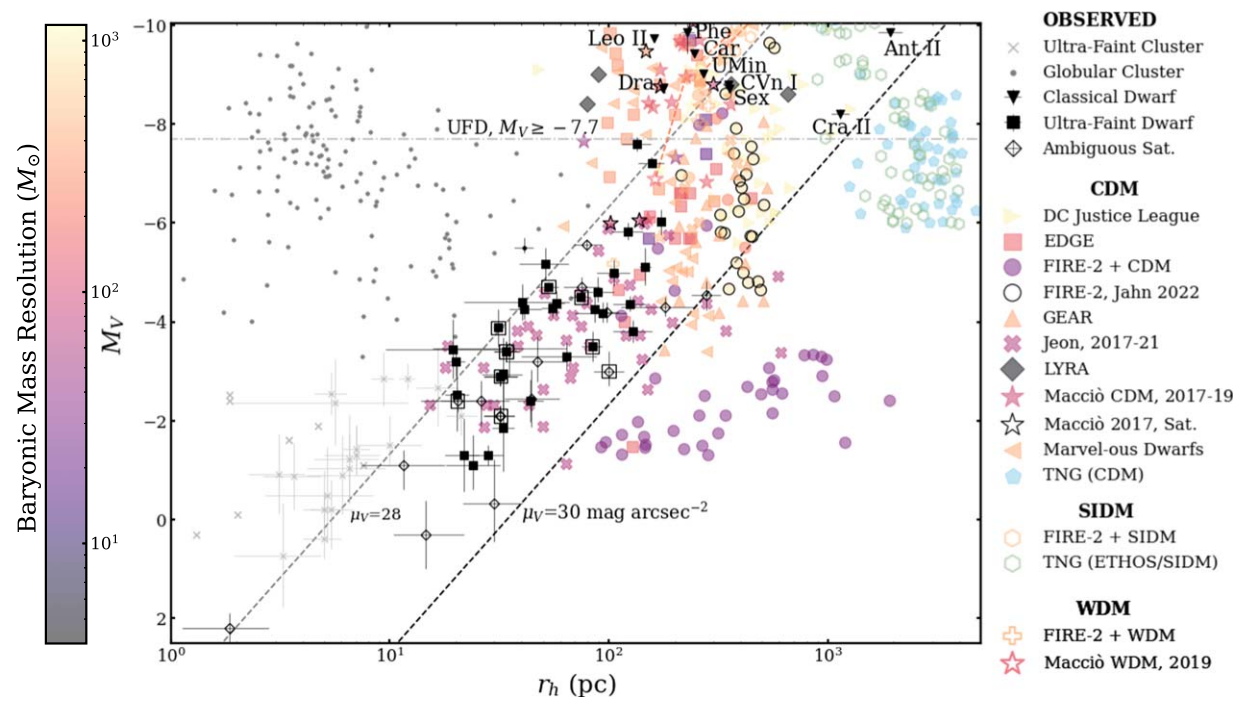


Figure 8. Absolute V-band magnitude, M_V , vs. azimuthally averaged half-light radius, r_h . The dashed light and dark gray diagonal lines represent constant surface-brightness values of 28 and 30 mag arcsec⁻², respectively. The dashed–dotted horizontal light gray line marks $M_V \ge -7.7$, often used as the delineation between classical and ultrafaint dwarfs (Simon 2019). Classical dwarfs (black inverted triangles) are labeled. Measurements of classical dwarfs, UFDs (black squares), and ambiguous satellites (open diamonds) are shown as black markers with error bars. LMC-associated satellites are additionally marked with a black square frame. Globular and "ultrafaint" clusters are shown as gray points and x's, respectively. All other markers are from simulations and colored by their baryonic particle mass resolution, except for the TNG points, which have a mass resolution $\sim 10^4 M_{\odot}$. If different environments were used within the same simulation grouping, we have marked the difference using black outlines. Simulated points using alternative DM models are shown as open symbols. The Macciò et al. (2019) WDM galaxies are connected to their corresponding CDM galaxies with coral dashed lines. Advances in simulations have led many groups to be able to generate galaxy analogs in and around the observed UFD space. Full references for the data are given in Appendix B, and references for the simulations are in Table 3.

2018; Sanati et al. 2023), Macciò et al. (2017), Macciò et al. (2019), and the Marvel-ous Dwarfs (Munshi et al. 2021) groups have also produced some UFDs that match the bright end of the observed population.

The fact that observed UFD properties are able to be matched by high-resolution simulations of isolated UFDs could suggest that environmental effects from the MW have not played a critical role in their size evolution. Additionally, the LMC-associated UFDs are matched by these isolated simulations. Their more recent infall (\sim 2 Gyr ago), paired with their lack of differences in the M_{V} - r_{h} space from the non-LMC-associated UFDs, further supports that the presence of the MW has had little overall consequence on the bulk of the current UFD size distribution.

Interestingly, in a study of the extended stellar populations of UFDs (i.e., member stars beyond 4 times r_h), Tau et al. (2024) found that at least 10 satellites with external populations had a wide range of magnitude and pericenter distances. This too suggests that interactions with the MW are *not* what dominates the distribution of UFD stars that we observe today.

Despite the overlap of simulations with the brighter UFDs, most simulations are unable to produce analogs of the most compact observed UFDs ($r_h \sim 30$ pc; e.g., Revaz 2023). Rather, they are creating UFDs with half-light radii up to a order of magnitude larger than observed. Revaz (2023) speculates that this could be due to resolution limits, spurious numerical heating, or improper feedback prescriptions, although the widespread nature of the pattern suggests there is no singular factor. In their own work using DM-only

simulations, Revaz (2023) found that minihalo mergers played a large role in the expansion of the simulated UFD sizes.

Conversely, it could be said that simulations are producing galaxies that are more diffuse than currently known observationally. This disparity can be revisited as new observatories come online, and we expand our knowledge of the low surface-brightness universe. Discoveries of larger, low surface-brightness UFDs could resolve the current discrepancy.

The simulations whose data we show in Figure 8 have a wide range of mass resolutions and distinct implementations of subgrid physics, which are necessary to form galaxies in a cosmological simulation, as the range of scales (e.g., individual supernovae, hereafter SNe, to Mpc-sized volumes) would be too computationally expensive otherwise. Despite using different combinations of free parameters, many simulation groups are still able to produce UFD analogs that fall within the same M_V – r_h space. For example, simulated UFDs with r_h between ~ 100 and 300 pc and $M_V \leqslant -4$ are produced by the DC Justice League (Applebaum et al. 2021), EDGE (Agertz et al. 2020; Orkney et al. 2021; Rey et al. 2022), FIRE-2 (Jahn et al. 2022; Wetzel et al. 2023), GEAR (Sanati et al. 2023; Jeon et al. 2017; Macciò et al. 2017, 2019), and the Marvel-ous Dwarfs (Munshi et al. 2021).

The consistently most compact UFDs ($r_h < 100$ pc) come from Jeon et al. (2021a, 2021b). Paired with their low luminosities ($M_V \geqslant -4$), these simulations are quite successful in reproducing the observed distribution of the LMC- and non-LMC-associated UFDs in the magnitude–size plane. These high-resolution simulations were run with a customized version of GADGET (Springel 2005), which used smoothed particle

 Table 3

 Selected UFD Simulation Parameters from Figure 8

			Simulation Description	ıs		
Simulation Set	$N_{ m gal}^{ m a}$	Hydro. Code	Baryonic Res. (M_{\odot})	Halo Mass ^c , $z = 0$ (M_{\odot})	Environment	References
			CDM			
DC Justice League	36	CHANGA	994	$1.1 \times 10^6 - 3.7 \times 10^9$	MW-like	1
EDGE	31	RAMSES-RT	20-300	$8.0 \times 10^{8} - 3.7 \times 10^{9}$	Isolated	2, 3, 4, 5
FIRE-2 + CDM	42	GIZMO	30-250	$7.0 \times 10^{8} - 9.0 \times 10^{9}$	Isolated	6, 7, 8, 9
FIRE-2, Jahn 2022	25	GIZMO	880	$(2.9-6.1) \times 10^8$	LMC-like	6, 10, 11
GEAR	19	GEAR ^b	380	3.0×10^{8} – 2.4×10^{9}	Isolated	12
Jeon 2017	6	Modified GADGET	465	$(1.5-4.0) \times 10^9$	Field	13
Jeon 2021	42	Modified GADGET	65	$(2.0-2.5) \times 10^8$	Field	14, 15
LYRA	4	AREPO	4	3.0×10^{8} – 2.8×10^{9}	Isolated	16
Macciò 2017, Cent.	9	GASOLINE	40, 135	$(1.7-5.7) \times 10^9$	Isolated overdensity	17
Macciò 2017, Sat.	6	GASOLINE	90, 305	4.5×10^{8} – 1.1×10^{10}	Isolated overdensity	17
Macciò 2019 (CDM)	4	GASOLINE-2	$2.4 \times 10^3 - 1.9 \times 10^4$	$(2.9-9.1) \times 10^9$	Isolated overdensity	18
Marvel-ous Dwarfs	32	CHANGA	420	2.6×10^{8} -4.5×10^{9}	Local Volume	19
TNG (CDM)	47	AREPO	4.2×10^{4}	$2.2 \times 10^7 - 2.8 \times 10^9$	Field	20
			SIDM			
FIRE-2 + SIDM	4	GIZMO	500	8.1×10^{9}	Isolated	21
TNG (ETHOS/SIDM)	52	AREPO	4.2×10^{4}	$1.9 \times 10^6 4.2 \times 10^9$	Field	22
			WDM			
FIRE-2 + WDM	3	GIZMO	500	$(6.7-8.5) \times 10^9$	Isolated	23
Macciò 2019 (WDM)	3	GASOLINE-2	$2.4 \times 10^3 - 1.9 \times 10^4$	$3.1 \times 10^9 - 1.3 \times 10^{10}$	Isolated overdensity	18

Notes. For each set of simulations shown in Figure 8, we list the set name, number of galaxies shown in the plot, the hydrodynamics code used, the baryonic resolution, the z=0 DM halo mass range, the environment in which the galaxies were simulated, and the appropriate references.

References. (1) Applebaum et al. (2021); (2) Agertz et al. (2020); (3) Rey et al. (2020); (4) Orkney et al. (2021); (5) Prgomet et al. (2022); (6) Fitts et al. (2017); (7) Hopkins et al. (2018); (8) Wheeler et al. (2019); (9) Wetzel et al. (2023); (10) El-Badry et al. (2018); (11) Jahn et al. (2022); (12) Sanati et al. (2023); (13) Jeon et al. (2017); (14) Jeon et al. (2021a); (15) Jeon et al. (2021b); (16) Gutcke et al. (2022); (17) Macciò et al. (2017); (18) Macciò et al. (2019); (19) Munshi et al. (2021); (20) Rose et al. (2023); (21) Robles et al. (2017); (22) J. Rose et al. (2024, in preparation); (23) Bozek et al. (2019).

hydrodynamics with a gas particle mass of 63 M_{\odot} . A variable softening length was used for the gas particles with a minimum length of \sim 3 pc. Individual Population III stars could be born out of pristine gas, while Population II stars were formed out of metal-enriched gas in complexes no less massive than 500 M_{\odot} to emulate the birth of stars out of molecular clouds.

The UFDs from the EDGE simulations (Agertz et al. 2020; Rey et al. 2020; Orkney et al. 2021; Prgomet et al. 2022) are slightly larger and more luminous than those of Jeon et al. (2021a, 2021b), but still fainter and more compact than many of the other simulated galaxies. Their properties relative to the Jeon et al. (2021a, 2021b) galaxies are reasonable as the EDGE UFDs inhabited DM halos that were up to an order of magnitude more massive than those hosting the UFDs in Jeon et al. (2021a, 2021b; see Table 3). The UFDs from the EDGE simulations track the observed magnitude-size relation well, overlapping with the LMC- and non-LMC-associated UFDs at the bright end $(M_V \leq -4)$. These high-resolution simulations were run with the RAMSES-RT adaptive mesh refinement code (Teyssier 2002; Rosdahl et al. 2013; Rosdahl & Teyssier 2015) at a variety of resolutions and with many variations in the baryonic physics.

In the UFD regime, besides the baryonic mass resolution, one could also consider the targeted halo mass at z = 0 for simulations as a possible factor in the final galaxy size. For

example, in a study specifically focused on reproducing the compactness of observed UFDs, Revaz (2023) used dark-matter-only (DMO) simulations to study how the initial size and later merger history of UFD building blocks affected the z=0 size of UFDs. They concluded that simulated UFDs with $r_h < 30$ pc can form from single minihalos with masses smaller than $4 \times 10^8 M_{\odot}$ at z=6 and initial sizes <15 pc.

Jeon et al. (2021a, 2021b) were able to hydrodynamically simulate UFDs on this size scale with halo masses $\langle 2.5 \times 10^8 M_{\odot}$. A few other simulations had halo masses below this (e.g., Applebaum et al. 2021; Rose et al. 2023; J. Rose et al., 2024, in preparation) but were unable to achieve the compactness. For Applebaum et al. (2021), this could be due to the difficulty in simulating UFDs in addition to a MW-mass scale galaxy, while, for TNG, their subgrid physics choices (as discussed further below) limited their minimum compactness.

The simulated galaxies that lie farthest from the observed sample and away from the bulk of the other simulations are the highest-resolution FIRE-2 galaxies from Wheeler et al. (2019), which have very low surface brightnesses ($\mu_V \gtrsim 30$ mag arcsec⁻²), and the TNG galaxies in both the CDM and ETHOS/SIDM cosmologies (Rose et al. 2023; J. Rose et al. 2024, in preparation), which have very large sizes

^a The number of galaxies shown in Figure 8, with an $M_V \gtrsim -10$ cut imposed.

^b GEAR was based on GADGET-2 (Springel 2005).

^c DM halo mass range (rounded to two significant figures) for the galaxies shown in Figure 8. Note that the mass range for the full simulation set could be larger.

Table 4Structural Parameters for Horologium I

		Hor	ologium I		
Parameter	Bechtol et al. (2015)	Koposov et al. (2015b) ^a	Muñoz et al. (2018)	Moskowitz & Walker (2020) ^b	This Work
$\overline{M_V}$	-3.5 ± 0.3	-3.4 ± 0.1	-3.55 ± 0.56	•••	-3.4 ± 0.2
		Exp	ponential		
R.A. (deg)		43.8820	43.8813 ± 25."65	•••	43.8759 ± 3"
decl. (deg)	•••	-54.1188	$-54.1160 \pm 20\rlap.{''}2$	•••	$-54.1174 \pm 3''$
$\theta_{\rm exp}~({\rm deg})$		Unconstrained	53 ± 27	•••	44 ± 7
$\epsilon_{ m exp}$		< 0.28	0.32 ± 0.13		0.26 ± 0.05
$a_{h, \exp}$ (arcmin)		$1.41^{+0.29}_{-0.13}$	1.71 ± 0.37		$1.70^{+0.16}_{-0.15}$
$a_{h,\text{exp}}$ (pc)		$33^{+6.8}_{-4.8}$	39.3 ± 8.5		$39.2^{+5.2}_{-4.7}$
		P	lummer		
R.A. (deg)	43.87	•••	43.8813 ± 25."65	43.882	43.8755 ± 3"
decl. (deg)	-54.11		$-54.1160 \pm 20\rlap.{''}2$	-54.119	$-54.1174 \pm 3''$
θ_p (deg)	Unconstrained	•••	57 ± 25	$66.59^{+13.41}_{-13.65}$	44 ± 6
ϵ_p	Unconstrained		0.27 ± 0.13	$0.14^{+0.06}_{-0.05}$	0.27 ± 0.05
$a_{h,p}$ (arcmin)	$2.4^{+3.0}_{-1.2}$		1.59 ± 0.31	1.67 ± 0.10	1.61 ± 0.13
$a_{h,p}$ (pc)	60^{+76}_{-30}		36.5 ± 7.1	$38.6^{+4.6}_{-3.9}$	$37.3^{+4.2}_{-4.7}$

Notes. Compilation of past literature measurements for Horologium I, which includes fits from both the exponential and Plummer models. Our parameters are quoted from the maximum-likelihood estimation, with the listed uncertainties corresponding to the 84th and 16th percentiles around the median of the distribution. The italic table section headers denote whether the parameters listed correspond to the Plummer or exponential models that were fit.

 $(r_h \gtrsim 10^3 \text{ pc}; \text{ although it should be remembered that we are not expecting TNG to be producing true UFD analogs).}$

The FIRE-2 galaxies in this group have $\sim 30 M_{\odot}$ baryonic particle resolution and were presented in Wheeler et al. (2019). Their larger sizes are not due to mass resolution or the force-softening scale, and the authors suggest that only the bright cores of UFDs are being captured by current observatories. When Wheeler et al. (2019) applied a surface-brightness detection limit of <30 mag arcsec⁻² and remeasured the apparent r_h and M_{\star} , their simulated analogs moved into the same space as observed UFDs.

As we were able to trace the morphologies of the dwarfs in our sample to an average surface brightness of $\mu_V = 31.2$ mag arcsec⁻², we expect that our measurements were not significantly biased by our imaging depth (see also the discussion at the end of Section 3.1). However, new observational facilities are set to come online in the next decade that should reach or exceed our photometric depth while covering the entirety of the dwarfs (e.g., the Vera C. Rubin Observatory/LSST, Ivezić et al. 2019; and the Roman Space Telescope, Spergel et al. 2015). As our HST fields are limited in their FOV, it will be interesting to see what these observatories may reveal about the extremities of these dwarf galaxies.

Of note, the Wheeler et al. (2019) FIRE-2 galaxies employed the same subgrid physics model as other FIRE-2 galaxies (e.g., the Jahn et al. 2022) in Figure 8 that are less diffuse for their magnitude. The two differences between these sets of FIRE-2 simulations were their mass resolutions and the environments in which the galaxies were simulated. The Wheeler et al. study considered UFDs in isolated dwarf galaxy halos, while the

work of Jahn et al. examined UFDs around an LMC-mass halo. The environment has previously been shown to affect DM halo properties such as concentration, where halos that formed earlier in cosmic time, when the Universe was more dense, have more highly concentrated density profiles (e.g., Wechsler et al. 2002). Additionally, for galaxies with the same peak halo masses, those that formed in more dense environments tended to have higher stellar masses than those that were isolated (Christensen et al. 2024).

It has not yet been explored whether there is a correlation for simulated UFD size (r_h) or light profile concentration with relation to the environment or formation time. As the target UFDs that we fit structural parameters for all had surface density profiles that were well described by exponential and/or Plummer profiles, they showed no signs of variation. A larger sample of observed UFDs with fewer FOV constraints could be used in tandem with simulations to investigate if the formation environment could have an impact on present-day morphological properties.

Focusing now on the TNG simulations, both sets of galaxies occupy similar spaces in the M_V – r_h plane, suggesting that the different DM models might not have a large effect on observable size. We also see that they tend to have larger r_h values, especially for the magnitude space that they occupy. This is due to how they implement their star formation and pressurization of the multiphase interstellar medium (ISM; e.g., Pillepich et al. 2018).

The IllustrisTNG model is unable to resolve SNe and uses a pressurized equation of state that does not allow the gas to cool below 10⁴ K, thus prohibiting collapse on smaller physical scales. As such, there is a limit to how compact the TNG dwarf

^a The values reported as a_h in arcminutes here are the values given as r_{maj} in Koposov et al. (2015b; Table 1) multiplied by 1.68, as their r_{maj} corresponded to the exponential scale length r_e .

^b The values reported as a_h in arcminutes here are the values given as $R_{h,1c}$ divided by $\sqrt{1-\epsilon_{1c}}$ in their Table 3, as their R_h is what they refer to as the "circularized projected half-light radii" equal to $a_h\sqrt{1-\epsilon_{1c}}$. Moskowitz & Walker (2020) do not report fitted R.A. and decl. values; thus, we list the values given in their Table 2.

Table 5
Structural Parameters for Horologium II

	Horologi	um II	
Parameter	Kim & Jerjen (2015)	Moskowitz & Walker (2020) ^a	This Work
$\overline{M_V}$	$-2.6^{+0.2}_{-0.3}$		-2.1 ± 0.2
	Expone	ntial	
R.A. (deg)	49.1337 ± 5"		49.1315 ± 4"
decl. (deg)	$-50.0180 \pm 5''$		$-50.0088 \pm 3''$
$\theta_{\rm exp}$ (deg)	127 ± 11		103^{+12}_{-14}
$\epsilon_{ m exp}$	$0.52^{+0.13}_{-0.17}$		$0.23^{+0.07}_{-0.08}$
$a_{h, \exp}$ (arcmin)	$2.09^{+0.44}_{-0.41}$	•••	1.63 ± 0.18
$a_{h,\text{exp}}$ (pc)	47 ± 10		$36.9^{+5.1}_{-5.4}$
	Plumn	ner	
R.A. (deg)	•••	49.134	49.1310 ± 4"
decl. (deg)		-50.0181	$-50.0090 \pm 3''$
$\theta_{\rm p}$ (deg)		$279.71^{+8.25}_{-189.75}$	103^{+11}_{-14}
$\epsilon_{ m p}$		0.40 ± 0.14	$0.23^{+0.07}_{-0.08}$
$a_{h,p}$ (arcmin)		$2.54^{+0.43}_{-0.53}$	$1.69^{+0.18}_{-0.17}$
$a_{h,p}$ (pc)		$58.1^{+13.8}_{-10.7}$	$38.4_{-5.5}^{+4.9}$

Note. Our parameters are quoted from the maximum-likelihood estimation, with the listed uncertainties corresponding to the 84th and 16th percentiles around the median of the distribution. The italic table section headers denote whether the parameters listed correspond to the Plummer or exponential models that were fit.

galaxies can be, motivating the need for simulations based on more resolved subgrid physics with explicit treatments of the ISM to explore alternative DM models.

While the TNG simulated galaxies shown in Figure 8 should not be used for observational predictions, they are a useful marker for seeing what well-tested cosmological models produce at these scales. The similarity in sizes for the TNG galaxies produced using CDM versus ETHOS/SIDM could also suggest that the galaxy formation model is dominant over the DM prescription.

5.4.2. Alternative Dark Matter Models

In Figure 8, there is a subset of points that come from simulations based on alternate DM models, such as WDM (e.g., Bozek et al. 2019; Macciò et al. 2019) and SIDM (e.g., Robles et al. 2017; J. Rose et al. 2024, in preparation). Within the M_V – r_h plane, there are not extreme differences apparent in the faint dwarf analogs created with different DM models. Below, we present a brief overview of the more in-depth literature studies that have compared these DM models on mass scales relevant to UFDs.

To leverage DMO simulations, we can first characterize any strong differences present between the DM models without the presence of baryons. Then, we can see if those differences persist in the fully hydrodynamic runs, or if the addition of baryons causes observational degeneracies. Comparisons of cold DMO

Table 6Structural Parameters for Hydra II

	Н	Iydra II	
	Martin et al.	Muñoz et al.	
Parameter	(2015)	(2018)	This Work
M_V	-4.8 ± 0.3	-4.60 ± 0.37	$-4.6^{+0.2}_{-0.3}$
	Exp	oonential	
R.A. (deg)	185.4254	$185.4251\pm13\rlap.{''}65$	$185.4279 \pm 4''$
decl. (deg)	-31.9853	$-31.9860 \pm 13\rlap.{''}7$	-31.9728^{+7}_{-6}
$\theta_{\rm exp}$ (deg)	28^{+40}_{-35}	13 ± 28	-10^{+9}_{-10}
$\epsilon_{ m exp}$	$0.01^{+0.19}_{-0.01}$	0.25 ± 0.16	$0.30^{+0.08}_{-0.09}$
$a_{h, \exp}$ (arcmin)	$1.7^{+0.3}_{-0.2}$	1.65 ± 0.39	$2.70^{+0.41}_{-0.38}$
$a_{h, \exp}$ (pc)	68 ± 11	64.3 ± 15.2	$105.6^{+17.9}_{-16.1}$
	P	lummer	
R.A. (deg)	•••	185.4251 ± 13."65	185.4286+4"
decl. (deg)		$-31.9860 \pm 13\rlap.{''}7$	-31.9728^{+9}_{-7} "
θ_p (deg)		16 ± 25	-9^{+8}_{-9}
ϵ_p		0.24 ± 0.16	0.30 ± 0.09
$a_{h,p}$ (arcmin)	•••	1.52 ± 0.28	$2.13^{+0.42}_{-0.35}$
$a_{h,p}$ (pc)	•••	59.2 ± 10.9	$83.3^{+17.1}_{-15.1}$

Note. Our parameters are quoted from the maximum-likelihood estimation, with the listed uncertainties corresponding to the 84th and 16th percentiles around the median of the distribution. The italic table section headers denote whether the parameters listed correspond to the Plummer or exponential models that were fit.

simulations to observations of dwarf spiral galaxies previously led to the "core-cusp" problem, where measured rotation curves implied the presence of cores, rather than the predicted steep density profiles $(\rho \propto r^{-1})$ (e.g., Flores & Primack 1994; Moore 1994). While there have since been explanations for this difference consistent with CDM (such as time-varying gravitational potentials, see, e.g., Pontzen & Governato 2012; Dutton et al. 2016; Orkney et al. 2021), alternative DM models have also been proposed to address the "core-cusp" and other challenges that Λ CDM seemingly faced on small (<1 Mpc) scales (see Bullock & Boylan-Kolchin 2017, for a review).

For example, SIDM-only simulations have been able to produce dwarf halos with constant-density cores ($r_c \sim 1~\rm kpc$) (e.g., Burkert 2000; Davé et al. 2001; Rocha et al. 2013; Robles et al. 2017). WDM-only simulations have also produced less centrally dense halos (e.g., Lovell et al. 2012; Shao et al. 2013), although some simulations predict cores closer to $\sim 10~\rm pc$ (Macciò et al. 2012), which would be insufficient for resolving the core-cusp problem. These three DM models thus have distinct signatures present when there are no baryons involved. As we rely on observations of baryonic matter for science, however, we must see what effect the addition of baryons has on these simulations.

Here, we focus on baryonic simulations that used fixed subgrid physics for both CDM and alternative DM runs. ²⁵ In comparing UFD analogs in CDM versus SIDM cosmologies, both FIRE-2 (Robles et al. 2017) and TNG (ETHOS/SIDM; J. Rose et al. 2024, in preparation) found similar M_{\star} - r_h relations between the two models. Additionally, cores were difficult to form in CDM, with only the most massive halo

^a The values reported as a_h in arcminutes here are the values given as $R_{h,1c}$ divided by $\sqrt{1-\epsilon_{1c}}$ in their Table 3, as their R_h is what they refer to as the "circularized projected half-light radii" equal to $a_h\sqrt{1-\epsilon_{1c}}$. Moskowitz & Walker (2020) do not report fitted R.A. and decl. values; thus, we list the values given in their Table 2.

²⁵ When discussing the simulations, unless specified as DM only, we are referring to the baryonic simulations based on the DM models.

Table 7Structural Parameters for Phoenix II

			Phoenix II			
Parameter	Bechtol et al. (2015) ^a	Koposov et al. (2015b) ^b	Muñoz et al. (2018)	Mutlu-Pakdil et al. (2018)	Moskowitz & Walker (2020) ^c	This Work
M_V	-3.7 ± 0.4	-2.8 ± 0.2	-3.30 ± 0.63	-2.7 ± 0.4	•••	$-2.9^{+0.2}_{-0.1}$
			Exponential			
R.A. (deg)	•••	354.9975	354.9960 ± 13."5	354.9928 ± 8."3	•••	354.9922 ± 3"
decl. (deg)	•••	-54.4060	-54.4115 ± 21.00	-54.4050 ± 5.7		$-54.4018 \pm 3''$
$\theta_{\rm exp}$ (deg)	•••	164 ± 54	-19 ± 15	156 ± 13		-34 ± 4
$\epsilon_{ m exp}$		$0.47^{+0.08}_{-0.29}$	0.62 ± 0.19	0.4 ± 0.1		0.44 ± 0.6
$a_{h, \exp}$ (arcmin)		$1.38^{+0.45}_{-0.20}$	1.60 ± 0.33	1.5 ± 0.3		$1.58^{+0.26}_{-0.23}$
$a_{h, \exp}$ (pc)		$34.3^{+10.7}_{-6.4}$	38.6 ± 8.0	37 ± 6		43.0^{+8}_{-7}
			Plummer			
R.A. (deg)	354.99		354.9960 ± 13"5		354.998	354.9919 ± 3"
decl. (deg)	-54.41		-54.4115 ± 21.00	•••	-54.406	$-54.4019 \pm 3''$
$\theta_p \text{ (deg)}$	Unconstrained		-20 ± 18		$285.28^{+15.31}_{-14.54}$	-33 ± 5
ϵ_p	Unconstrained		0.67 ± 0.22	•••	$0.27^{+0.11}_{-0.10}$	0.44 ± 0.06
$a_{h,p}$ (arcmin)	$1.2^{+1.2}_{-1.2}$	•••	1.49 ± 0.53	•••	$1.85^{+0.30}_{-0.33}$	$1.50^{+0.20}_{-0.17}$
$a_{h,p}$ (pc)	33^{+20}_{-11}	•••	36.0 ± 12.8		$45.1^{+9.5}_{-7.8}$	$40.8^{+5.5}_{-6.2}$

Notes. Our parameters are quoted from the maximum-likelihood estimation, with the listed uncertainties corresponding to the 84th and 16th percentiles around the median of the distribution. The italic table section headers denote whether the parameters listed correspond to the Plummer or exponential models that were fit.

Table 8
Structural Parameters for Sagittarius II

			Sagittarius II		
Parameter	Laevens et al. (2015a)	Mutlu-Pakdil et al. (2018)	Longeard et al. (2020)	Moskowitz & Walker (2020) ^a	This Work
$\overline{M_V}$	-5.2 ± 0.4	-4.2 ± 0.1	-5.7 ± 0.1		-5.3 ± 0.2
			Exponential		
R.A. (deg)	298.1688	298.1647 ± 3."0	298.16628 ± 3."6	•••	298.1664 ± 2"
decl. (deg)	-22.0681	$-22.0651 \pm 2\rlap{.}''2$	$-22.89633 \pm 3.0\%$		$-22.0641\pm2''$
$\theta_{\rm exp}$ (deg)	72^{+28}_{-20}	Unconstrained	103^{+28}_{-17}		98^{+43}_{-30}
$\epsilon_{ m exp}$	$0.23^{+0.17}_{-0.23}$	< 0.1	0.0, <0.12 at 95% CL		0.03, <0.09 at 95% CL
$a_{h, \exp}$ (arcmin)	$2.0_{-0.3}^{+0.4}$	1.6 ± 0.1	1.7 ± 0.05		1.94 ± 0.08
$a_{h,\text{exp}}$ (pc)	38^{+8}_{-7}	32 ± 1	$35.5^{+1.4}_{-1.2}$		39 ± 4
			Plummer		
R.A. (deg)				298.169	298.1664 ± 2"
decl. (deg)				-22.068	$-22.0642\pm2''$
$\theta_p (\deg)$		•••		$74.90^{+14.69}_{-13.02}$	96^{+50}_{-32}
ϵ_p				$0.24^{+0.10}_{-0.09}$	0.03, <0.08 at 95% CL
$a_{h,p}$ (arcmin)				$1.87^{+0.19}_{-0.22}$	$1.85^{+0.07}_{-0.08}$
$a_{h,p}$ (pc)				$36.7_{-4.3}^{+5.1}$	37 ± 4

Note. Our parameters are quoted from the maximum-likelihood estimation, with the listed uncertainties corresponding to the 84th and 16th percentiles around the median of the distribution. The italic table section headers denote whether the parameters listed correspond to the Plummer or exponential models that were fit.

^a The values reported as a_h in arcminutes here are the values given as r_h (deg) in Bechtol et al. (2015; Table 1), multiplied by 60. The values reported as a_h in parsecs here are the values given as $r_{1/2}$ (pc) in Bechtol et al. (2015) Table 2.

^b The values reported as a_h in arcminutes here are the values given as r_{maj} in Koposov et al. (2015b; Table 1) multiplied by 1.68, as their r_{maj} corresponded to the exponential scale length r_e .

^c The values reported as a_h in arcminutes here are the values given as $R_{h,1c}$ divided by $\sqrt{1-\epsilon_{1c}}$ in their Table 3, as their R_h is what they refer to as the "circularized projected half-light radii" equal to $a_h\sqrt{1-\epsilon_{1c}}$. Moskowitz & Walker (2020) do not report fitted R.A. and decl. values; thus, we list the values given in their Table 2.

^a The values reported as a_h in arcminutes here are the values given as $R_{h,1c}$ divided by $\sqrt{1-\epsilon_{1c}}$ in their Table 3, as their R_h is what they refer to as the "circularized projected half-light radii" equal to $a_h\sqrt{1-\epsilon_{1c}}$. Moskowitz & Walker (2020) do not report fitted R.A. and decl. values; thus, we list the values given in their Table 2.

Table 9
Structural Parameters for Triangulum II

		Tr	iangulum II		
Parameter	Laevens et al. (2015b)	Carlin et al. (2017)	Muñoz et al. (2018)	Moskowitz & Walker (2020) ^a	This Work
$\overline{M_V}$	-1.8 ± 0.5	-1.2 ± 0.4	-1.60 ± 0.76		$-1.4^{+0.3}_{-0.2}$
		E	Exponential		
R.A. (deg)	33.3225	33.3223 ± 14."4	33.3252 ± 14"55		33.3152 ± 8"
decl. (deg)	36.1784	$36.1719 \pm 9\rlap.{''}7$	$36.1702 \pm 19\rlap.{''}0$	•••	36.1704^{+8}_{-9} "
$\theta_{\rm exp}$ (deg)	56^{+16}_{-24}	73 ± 17	28 ± 19	•••	81^{+30}_{-39}
$\epsilon_{ m exp}$	$0.21^{+0.17}_{-0.21}$	0.3 ± 0.1	0.48 ± 0.17		$0.15^{+0.12}_{-0.10}$
$a_{h, \exp}$ (arcmin)	$3.9^{+1.1}_{-0.9}$	2.5 ± 0.3	2.34 ± 0.58		$3.50^{+0.59}_{-0.65}$
$a_{h,\text{exp}}$ (pc)	34^{+9}_{-8}	21 ± 4	20.4 ± 5.1		$29.0_{-5.4}^{+5.2}$
			Plummer		
R.A. (deg)	•••		33.3252 ±1"55	33.323	33.3155 ± 9"
decl. (deg)	•••		$36.1702 \pm 19\rlap.{''}0$	36.1783	36.1691^{+10}_{-12} "
θ_p (deg)	•••		44 ± 18	$300.72^{+27.55}_{-222.65}$	79^{+28}_{-38}
ϵ_p			0.46 ± 0.16	$0.26^{+0.13}_{-0.10}$	$0.15^{+0.12}_{-0.10}$
$a_{h,p}$ (arcmin)			1.99 ± 0.49	$1.80^{+0.30}_{-0.33}$	$3.25^{+0.51}_{-0.59}$
$a_{h,p}$ (pc)			17.4 ± 4.3	$16.0^{+3.0}_{-2.7}$	$27.0_{-4.9}^{+4.5}$

Note. Our parameters are quoted from the median, with the listed uncertainties corresponding to the 84th and 16th percentiles around the median of the distribution. The italic table section headers denote whether the parameters listed correspond to the Plummer or exponential models that were fit.

forming a core in the FIRE-2 runs and no halos forming cores in the TNG (CDM) runs (Rose et al. 2023). The SIDM halos did form cores, although the UFD core sizes and profiles were not significantly different from those formed in the SIDM-only runs. This suggests that the baryons had minimal effects on the DM structure of the dwarf galaxies considered. Robles et al. (2017) suggested that the observation of field dwarf with a DM core size similar to its r_h and a stellar mass $\lesssim 3 \times 10^6 M_{\odot}$ could support the need for a new DM paradigm.

For the simulated dwarfs in CDM versus WDM, Bozek et al. (2019; using FIRE-2 subgrid physics) and Macciò et al. (2019; using Numerical Investigation of a Hundred Astrophysical Objects, hereafter NIHAO, subgrid models; Wang et al. 2015) both found that the WDM galaxies formed the bulk of their stellar mass in the past ~4 Gyr. Bozek et al. (2019) proposed that observations of UFDs with more than 80% of their stellar mass formed in the last 4 Gyr would support the WDM model.

Both groups also found that, in general, the final WDM density profiles of halos hosting galaxies were less centrally dense than the halos in CDM, although baryonic feedback processes had a greater effect overall in lowering the central densities in the CDM runs; greater stellar mass and star formation efficiency were also correlated with greater central density reduction. Macciò et al. (2019) additionally predicted WDM halos hosting galaxies with $M_{\star} < 10^6$ would retain their cuspy profiles. Thus, the authors suggested that the unambiguous detection of a core in a UFD would require a more drastic change to the standard model. Bozek et al. (2019) used the WDM resonantly produced sterile neutrino particle model while Macciò et al. (2019) chose a WDM particle mass of 3 keV; however, both concluded that observables such as galaxy mass, shape, size, and velocity dispersion would not be useful in distinguishing between a CDM or WDM universe. These two studies produced very few simulated galaxies with

 Table 10

 Past Literature Measurements for Grus II from the Plummer Model Fits

Grus II					
Parameter	Drlica-Wagner et al. (2015)	Moskowitz & Walker (2020) ^a	Simon et al. (2020)		
M_V	-3.9 ± 0.22		-3.5 ± 0.3		
	Pl	ummer			
R.A. (deg)	331.02		331.025^{+32}_{-29}		
decl. (deg)	-46.44	-46.44	$-46.422\pm22''$		
$\theta_{\rm p}$ (deg)	Unconstrained	$67.05^{+228.74}_{-26.25}$	Unconstrained		
$\epsilon_{ m p}$	< 0.2	$0.12^{+0.06}_{-0.05}$	< 0.21		
$a_{h,p}$ (arcmin)	$6.0^{+0.9}_{-0.5}$	$7.80^{+0.56}_{-0.58}$	5.9 ± 0.5		
$a_{h,p}$ (pc)	93 ± 14	$121.5_{-13.89}^{15.23}$	94 ± 9		

Note. The italic table section headers denote whether the parameters listed correspond to the Plummer or exponential models that were fit.

 $M_V \geqslant -10$, however; so it would be informative to have a larger sample size of galaxies from WDM simulations specifically targeting the UFD-mass regime.

Finally, Fitts et al. (2019)²⁶ compared the effects of FIRE-2 baryonic physics on WDM, SIDM, and CDM, as well as two

^a The values reported as a_h in arcminutes here are the values given as $R_{h,1c}$ divided by $\sqrt{1-\epsilon_{1c}}$ in their Table 3, as their R_h is what they refer to as the "circularized projected half-light radii" equal to $a_h\sqrt{1-\epsilon_{1c}}$. Moskowitz & Walker (2020) do not report fitted R.A. and decl. values; thus, we list the values given in their Table 2.

^a The values reported as a_h in arcminutes here are the values given as $R_{h,1c}$ divided by $\sqrt{1-\epsilon_{1c}}$ in their Table 3, as their R_h is what they refer to as the "circularized projected half-light radii" equal to $a_h\sqrt{1-\epsilon_{1c}}$. Moskowitz & Walker (2020) do not report fitted R.A. and decl. values; however, the literature values that they list in their Table 2 for this target do not match other studies. Their listed R.A. value does match up with other reported decl. values, so we do include that here.

²⁶ The simulated data unique to this study are not in Figure 8 as they were not available.

Table 11
Past Literature Measurements for Reticiulum II from the Exponential and Plummer Model Fits

			Reticulum II		
Parameter	Bechtol et al. (2015) ^a	Koposov et al. (2015b) ^b	Muñoz et al. (2018)	Mutlu-Pakdil et al. (2018)	Moskowitz & Walker (2020)
$\overline{M_V}$	-3.6 ± 0.1	-2.7 ± 0.1	-3.88 ± 0.38	-3.1 ± 0.1	•••
			Exponential		
R.A. (deg)		53.9256	53.9203 ± 24."45	53.9493 ± 24."8	•••
decl. (deg)	•••	-54.0492	-54.0513 ± 7.9	$-54.0466 \pm 9\rlap.{''}1$	•••
$\theta_{\rm exp}$ (deg)	•••	71 ± 1	62 ± 2	68 ± 2	•••
$\epsilon_{ m exp}$		$0.59^{+0.02}_{-0.03}$	0.56 ± 0.03	0.6 ± 0.1	
$a_{h, \exp}$ (arcmin)		$5.66^{+0.39}_{-0.22}$	5.41 ± 0.18	6.3 ± 0.4	
$a_{h,\text{exp}}$ (pc)		50^{+6}_{-5}	47.2 ± 1.6	58 ± 4	
			Plummer		
R.A. (deg)	53.92		53.9203 ± 24."45	•••	53.925
decl. (deg)	-54.05		-54.0513 ± 7.9		-54.049
$\theta_p \text{ (deg)}$	72 ± 7	•••	70 ± 2	•••	69.51 ± 0.80
ϵ_p	$0.6^{+0.1}_{-0.2}$		0.58 ± 0.02	•••	0.60 ± 0.01
$a_{h,p}(arcmin)$	6.0 ± 0.6		5.52 ± 0.19		6.56 ± 0.15
$a_{h,p}(pc)$	55 ± 5	•••	48.2 ± 1.7	•••	$57.9^{+5.6}_{-5.3}$

Notes. The italic table section headers denote whether the parameters listed correspond to the Plummer or exponential models that were fit.

models combining SIDM and WDM. The authors found that the simulated dwarfs across their models had similar stellar half-mass radii to observed dwarf galaxies in the Local Field, and that the $r_{1/2}$ – M_{\star} relation (where $r_{1/2}$ is the 3D half-mass-radius) did not show different trends based on the DM model used. Similarly to the comparisons above, Fitts et al. (2019) found that the addition of baryonic physics made the DM density profile differences that were evident in the DMO-simulated halos less apparent.

In their chosen comparison plane of $V_{1/2}$ (the circular velocity at $r_{1/2}$) versus $r_{1/2}$, all five models (CDM, SIDM, WDM, and two SIDM+WDM) yielded similar results that agreed with observations. However, the alternate DM runs produced dwarfs with lower central densities than those in CDM for $M_{\star} \sim 10^6 M_{\odot}$. Fitts et al. (2019) suggested that measurements of circular velocities for the inner regions (<400 pc) of less massive dwarfs could be a strong discriminator for CDM versus an alternative DM. The authors concluded that a larger sample size of simulated dwarfs in this mass regime will be needed for a more thorough exploration.

The studies discussed above used the FIRE-2, IllustrisTNG, and NIHAO subgrid models, but it would be informative to see how the baryonic physics implementations of other simulation groups interact with alternative DM models on faint dwarf galaxy mass scales. These could provide suggestions for additional observational probes for differentiating between the proposed natures of DM.

5.4.3. The Low Surface-brightness Future

As the next generation of observing facilities come online (e.g., Euclid, Racca et al. 2016; Vera C. Rubin Observatory/

LSST, Ivezić et al. 2019; Roman Space Telescope, Spergel et al. 2015), we can expect even more low surface-brightness stellar populations to be discovered. For example, Mutlu-Pakdil et al. (2021) simulated the expected performance of the Subaru Hyper Suprime-Cam (Miyazaki et al. 2018) and Rubin, forecasting that we should obtain a "secure census" of galaxies out to 1.5 Mpc with $M_V \lesssim -7$ with $\mu_{V,0} \sim 30$ mag arcsec⁻². Similar investigations for resolved stellar streams with Roman (Pearson et al. 2019) and ultradiffuse galaxies (UDGs) with LSST depth (Newton et al. 2023) have also been conducted, and the authors are optimistic about the populations awaiting discovery within our Local Volume. Pearson et al. (2019) predicted that we will be able to detect resolved stellar streams from globular clusters out to \sim 3.5 Mpc, and Newton et al. (2023) predicted that there are \sim 12 isolated UDGs within 2.5 Mpc of the Local Group that should be observable in future deep surveys.

As an additional note, from examining this section of the M_V – r_h plane, there appears to be a deficit in the number of observed MW satellites with an M_V between -6 and -8. This is the same feature in the luminosity function that Bose et al. (2018) suggested may represent the dividing line between dwarfs that were quenched by reionization and those that were able to continue forming stars at later times. Manwadkar & Kravtsov (2022) also highlight this "break" in their GRUMPY semianalytic model and speculated that, as the census of Local Volume satellite galaxies grows more complete, we can probe reionization by further characterizing the abundance of UFDs and how sensitive they must have been to the ionizing radiation from that epoch.

We will likely need a greater sample size to determine if this deficit is anything besides a random fluctuation. Still, we might expect at least one MW satellite to be discovered with

^a The values reported as a_h in arcminutes here are the values given as r_h (deg) in Bechtol et al. (2015; Table 1), multiplied by 60. The values reported as a_h in parsecs here are the values given as $r_{1/2}$ (pc) in Bechtol et al. (2015) Table 2.

^b The values reported as a_h in arcminutes here are the values given as r_{maj} in Koposov et al. (2015b; Table 1) multiplied by 1.68, as their r_{maj} corresponded to the exponential scale length r_e .

^c The values reported as a_h in arcminutes here are the values given as $R_{h,1c}$ divided by $\sqrt{1-\epsilon_{1c}}$ in their Table 3, as their R_h is what they refer to as the "circularized projected half-light radii" equal to $a_h \sqrt{1-\epsilon_{1c}}$. Moskowitz & Walker (2020) do not report fitted R.A. and decl. values; thus, we list the values given in their Table 2.

Table 12
Past Literature Measurements for Tucana II from the Exponential and Plummer Model Fits

	Tuc	cana II	
Parameter	Bechtol et al. (2015) ^a	Koposov et al. (2015b) ^b	Moskowitz & Walker (2020) ^c
M_V	-3.9 ± 0.2	-3.8 ± 0.1	•••
	Expo	onential	
R.A. (deg)	•••	342.9796	•••
decl. (deg)		-58.5689	
$\theta_{\rm exp}$ (deg)		107 ± 18	
$\epsilon_{ m exp}$		$0.39^{+0.10}_{-0.20}$	
$a_{h, \exp}$ (arcmin)	•••	$12.89^{+1.71}_{-1.98}$	•••
$a_{h,\text{exp}}$ (pc)		217^{+40}_{-37}	
	Plı	ımmer	
R.A. (deg)	343.06		342.98
decl. (deg)	-58.57		-58.57
$\theta_p \text{ (deg)}$	Unconstrained		$274.02^{+6.81}_{-187.37}$
ϵ_p	Unconstrained		$0.34^{+0.07}_{-0.08}$
$a_{h,p}$ (arcmin)	7.2 ± 1.8		$13.48^{+1.10}_{-1.20}$
$a_{h,p}$ (pc)	120 ± 30		$230.1^{+31.0}_{-27.7}$

Notes. The italic table section headers denote whether the parameters listed correspond to the Plummer or exponential models that were fit.

 $100 < r_h < 400$ pc, as it would have a surface brightness above current and projected detection limits. Many hydrodynamic simulations have been able to produce galaxies in this magnitude range, and while there have been other Local Group galaxies discovered in that $M_V - r_h$ parameter space (e.g., McConnachie 2012), most of the currently known MW UFDs seem to be fainter than $M_V = -6$.

There are further details to be studied concerning the faint and low surface-brightness populations that we have recently discovered. For example, there are still several stellar systems (e.g., Hor II, Hya II, Phe II, Tri II) whose status as galaxies (rather than star clusters) has yet to be confirmed via spectroscopy. The Baumgardt et al. (2022) mass segregation technique has provided an alternative, however, and concluded that Hor II, Phe II, and Tri II are likely dwarf galaxies. The Fu et al. (2023) HST photometric metallicity study has also offered support via metallicity dispersion values for the classification of Hya II and Phe II as galaxies. The targets that we have labeled "ultrafaint clusters" also merit further studies, as not all have been conclusively ruled out as being DM dominated (e.g., Cerny et al. 2021a, 2021b, 2023c). Additionally, studies of faint dwarf stellar halos (Jensen et al. 2024) and UFD stars at distant radii (e.g., Tuc II; Chiti et al. 2021) suggest that deeper imaging of the fields around UFDs could reveal more about

Table 13
Past Literature Measurements for Tucana IV from the Plummer Model Fits

	T	ucana IV	
Parameter	Drlica-Wagner et al. (2015)	Moskowitz & Walker (2020) ^a	Simon et al. (2020)
$\overline{M_V}$	-3.5 ± 0.28		$-3.0^{+0.3}_{-0.4}$
	F	Plummer	
R.A. (deg)	0.73	0.73	0.717^{+50}_{-76}
decl. (deg)	-60.85	-60.85	-60.830^{+36}_{-40}
$\theta_{\rm p}$ (deg)	11 ± 9	$333.32^{+9.26}_{-54.63}$	27^{+9}_{-8}
$\epsilon_{ m p}$	0.4 ± 0.1	$0.35^{+0.07}_{-0.09}$	$0.39^{+0.07}_{-0.10}$
$a_{h,p}$ (arcmin)	$11.8^{+2.2}_{-1.8}$	$9.20^{+0.96}_{-1.05}$	$9.3^{+1.4}_{-0.9}$
$a_{h,p}$ (pc)	167^{+35}_{-30}	$129.2^{+19.3}_{-16.8}$	127^{+22}_{-16}

Note. The italic table section headers denote whether the parameters listed correspond to the Plummer or exponential models that were fit.

previous tidal interactions or whether they formed through the merger of smaller stellar systems (e.g., Goater et al. 2024). The depth and areal coverage of the surveys to come will be critical in our characterization and understanding of the low surface-brightness universe.

6. Summary and Conclusions

In this paper, we have presented new PSF photometry for 10 targets from the HST Treasury GO-14734 (PI: N. Kallivayalil): Grus II, Horologium I, Horologium II, Hydra II, Phoenix II, Reticulum II, Sagittarius II, Triangulum II, Tucana II, and Tucana IV. We have tested the ability to obtain structural parameter and M_V measurements from HST imaging with limited fields of view and recovered a_h measurements within 1σ of recent literature values for $\sim 40\%$ of the cases. While complications in the image data made these measurements difficult for several objects, all of our a_h measurements agree within 3σ of published values.

We have shown that there is no systematic difference in the M_{V} - r_{h} relationship for UFDs associated with the LMC versus those that are not. We examined the current state of dwarf galaxy simulations and found that several groups have been able to create analogs that are broadly consistent with the observed UFDs in the magnitude-size plane. We also considered whether *where* observed UFDs fall in the M_{V} - r_{h} plane would be useful in constraining the nature of DM. In comparing simulated galaxies from SIDM (Robles et al. 2017; J. Rose et al. 2024, in preparation), WDM (Bozek et al. 2019; Macciò et al. 2019), and CDM (see Table 3 for full citations) in the M_{V} - r_{h} space, we found no consistent trends based on the DM cosmology.

As we found no clear discriminator that would support one DM cosmology over another in the M_V – r_h plane, we reviewed and compared the predicted observables from the literature. From examining the results and conclusions of alternative DM studies from different simulation groups (although see Fitts et al. 2019, for an outstanding comparison within the FIRE-2 group), two clear observables that would strongly support a

^a The values reported as a_h in arcminutes here are the values given as r_h (deg) in Bechtol et al. (2015; Table 1), multiplied by 60. The values reported as a_h in parsecs here are the values given as $r_{1/2}$ (pc) in Bechtol et al. (2015; Table 2). ^b The values reported as a_h in arcminutes here are the values given as $r_{\rm maj}$ in Koposov et al. (2015b; Table 1) multiplied by 1.68, as their $r_{\rm maj}$ corresponded to the exponential scale length r_e .

^c The values reported as a_h in arcminutes here are the values given as $R_{h,1c}$ divided by $\sqrt{1-\epsilon_{1c}}$ in their Table 3, as their R_h is what they refer to as the "circularized projected half-light radii" equal to $a_h\sqrt{1-\epsilon_{1c}}$. Moskowitz & Walker (2020) do not report fitted R.A. and decl. values; thus, we list the values given in their Table 2.

^a The values reported as a_h in arcminutes here are the values given as $R_{h,1c}$ divided by $\sqrt{1-\epsilon_{1c}}$ in their Table 3, as their R_h is what they refer to as the "circularized projected half-light radii" equal to $a_h\sqrt{1-\epsilon_{1c}}$. Moskowitz & Walker (2020) do not report fitted R.A. and decl. values; thus, we list the values given in their Table 2.

non-CDM cosmology are (1) a UFD SFH with \gtrsim 80% of its stellar mass formed in the last 4 Gyr, which would agree with predictions from multiple WDM simulations (Bozek et al. 2019; Macciò et al. 2019), and (2) the presence of a core in a UFD with $M_{\star} \lesssim 10^6 M_{\odot}$, as current simulations suggest that UFDs of that mass would retain their cusps (Robles et al. 2017; Fitts et al. 2019; Macciò et al. 2019). Nonetheless, current hydrodyanmical simulations have generally been presenting baryonic solutions for the classical issues that CDM has faced on small scales (e.g., Sales et al. 2022), and a paradigm shift in the near-future would require substantial evidence.

Statistically robust samples of simulated dwarfs produced across different DM models will be necessary to more thoroughly explore the impact that the underlying DM cosmology has on tangible properties. Additionally, as more simulation groups explore alternative DM models, we can see if those, in combination with their subgrid physics implementations, suggest different observable relations that could be used to constrain DM properties. Finally, as new observing facilities come online and we begin to go beyond current survey depth limits, we will have more opportunities to discover and further characterize stellar populations in this low surface-brightness regime.

Acknowledgments

We thank the anonymous referee for the thoughtful comments and suggestions to help clarify this manuscript. H.R. would like to thank Peter B. Stetson, Tom Brown, Taylor Hoyt, and Rachael Beaton for useful discussions about DAOPHOT. H.R. acknowledges support from the Jefferson Scholars Foundation Dissertation Year Fellowship, the Hilliard

Family, and the Virginia Space Grant Consortium Graduate Research STEM Fellowship. C.T.G. acknowledges support from the Owens Family Foundation. This work was based on observations with the NASA/ESA Hubble Space Telescope obtained from the Mikulski Archive for Space Telescopes at the Space Telescope Science Institute (STScI). The specific observations analyzed can be accessed via 10.17909/tvwk-ye33. STScI is operated by the Association of Universities for Research in Astronomy, Inc., under NASA contract NAS5-26555. Support to MAST for these data is provided by the NASA Office of Space Science via grant NAG5-7584 and by other grants and contracts. This research has made use of NASA's Astrophysics Data System.

Facility: HST (ACS, WFC3).

Software: Aladin (Bonnarel et al. 2000), Astrodrizzle (Fruchter & Hook 2002; STScI Development Team 2012; Avila et al. 2015), Astropy (Astropy Collaboration et al. 2013, 2018, 2022), corner.py (Foreman-Mackey 2016), DAOPHOT-II (Stetson 1987, 1992), dustmaps (Green 2018), emcee (Foreman-Mackey et al. 2013), Jupyter Notebook (Kluyver et al. 2016), Matplotlib (Hunter 2007), Numpy (Harris et al. 2020), photutils (Bradley et al. 2020), scikit-learn (Pedregosa et al. 2011), Scipy (Virtanen et al. 2020), stsynphot (STScI Development Team 2020), synphot (STScI Development Team 2018).

Appendix A Additional Corner Plots

This appendix contains the corner plots for Horologium II (Figure 9), Hydra II (Figure 10), Phoenix II (Figure 11), Sagittarius II (Figure 12), and Triangulum II (Figure 13).

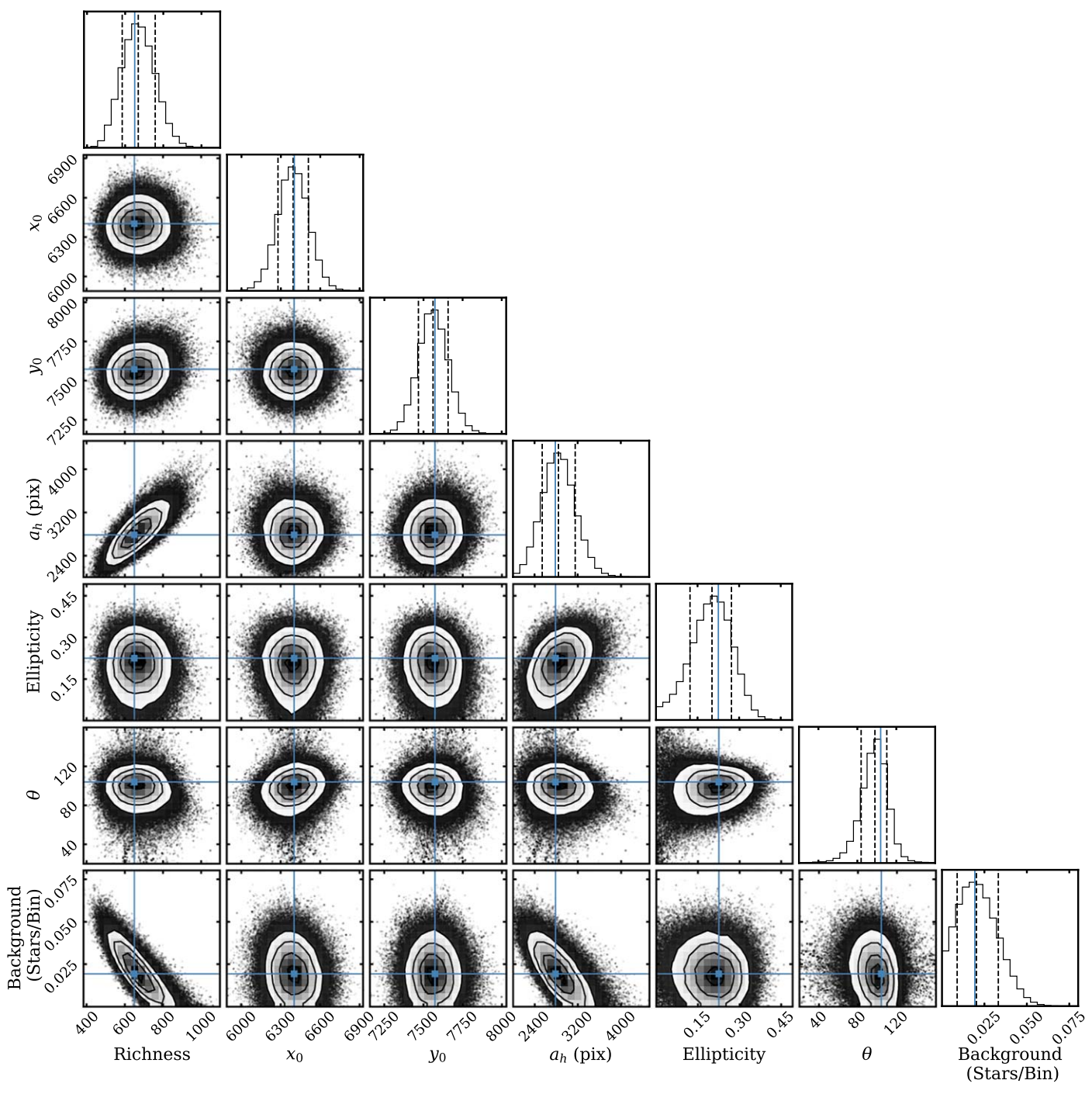


Figure 9. The posterior distributions of the seven-parameter structural fit for Hor II using the exponential model. The three black vertical dashed lines represent the 16th, 50th, and 84th percentiles. The blue lines and markers show the maximum-likelihood values.

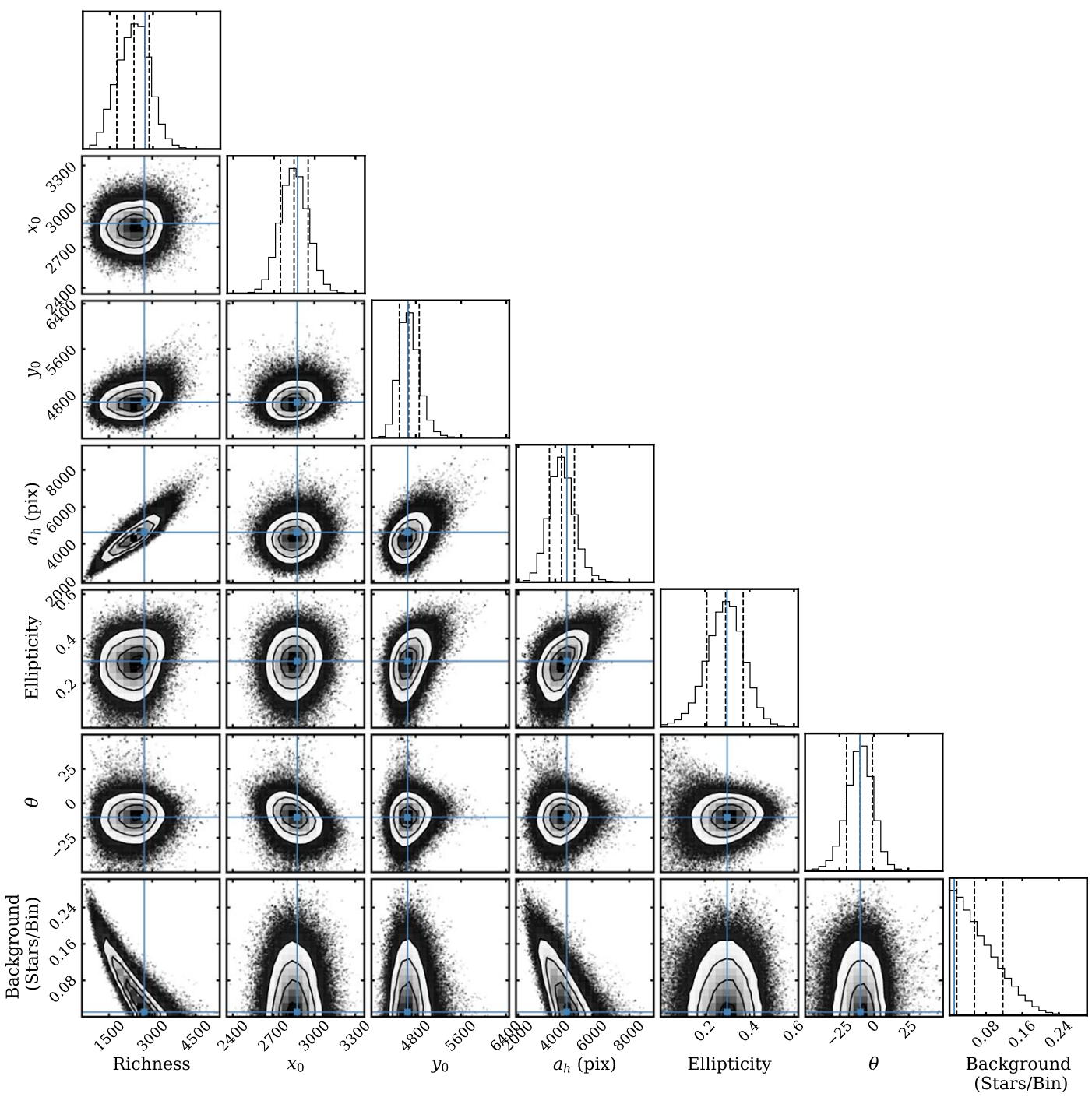


Figure 10. The posterior distributions of the seven-parameter structural fit for Hya II using the exponential model. The three black vertical dashed lines represent the 16th, 50th, and 84th percentiles. The blue lines and markers show the maximum-likelihood values.

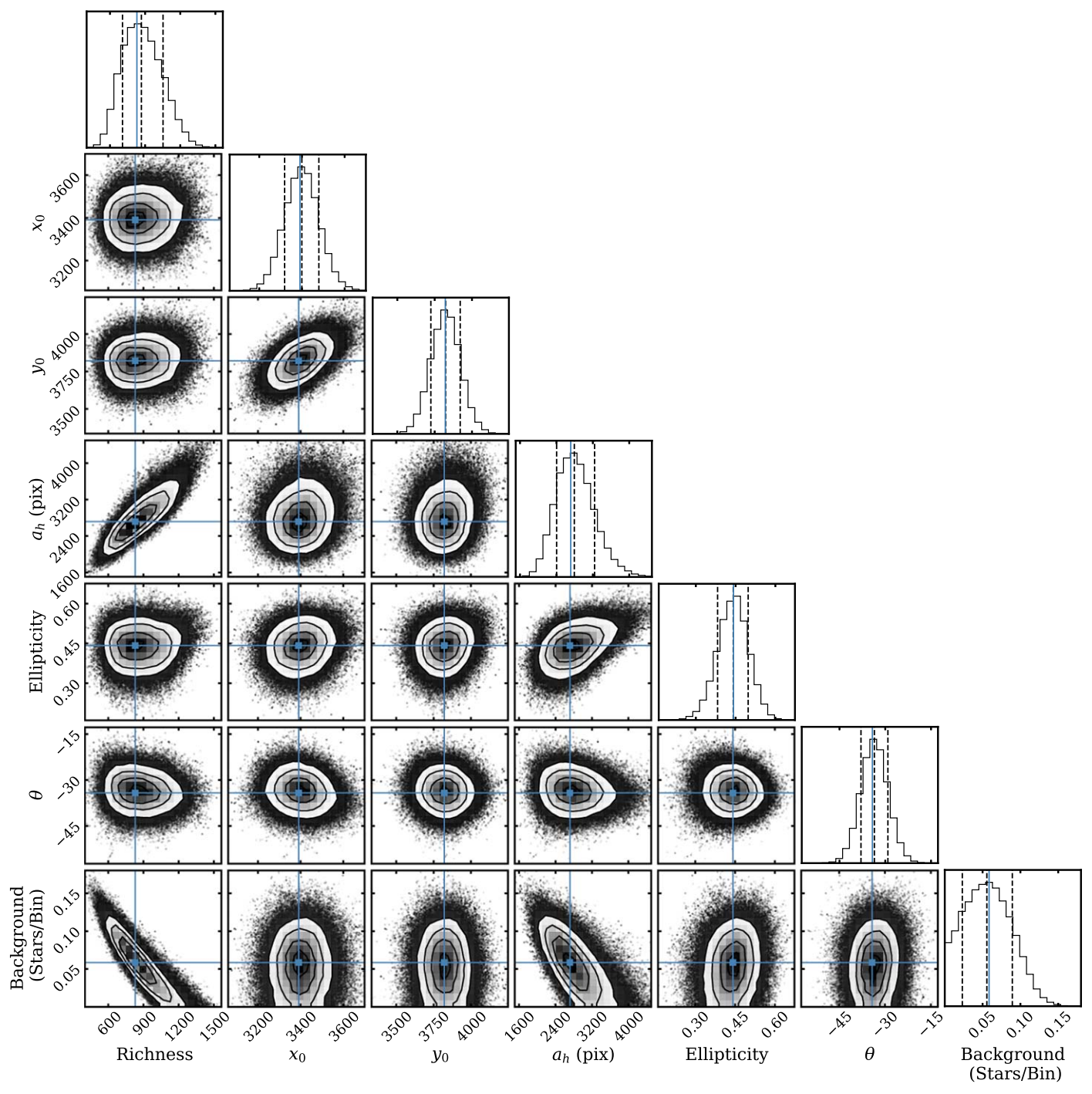


Figure 11. The posterior distributions of the seven-parameter structural fit for Phe II using the exponential model. The three black vertical dashed lines represent the 16th, 50th, and 84th percentiles. The blue lines and markers show the maximum-likelihood values.

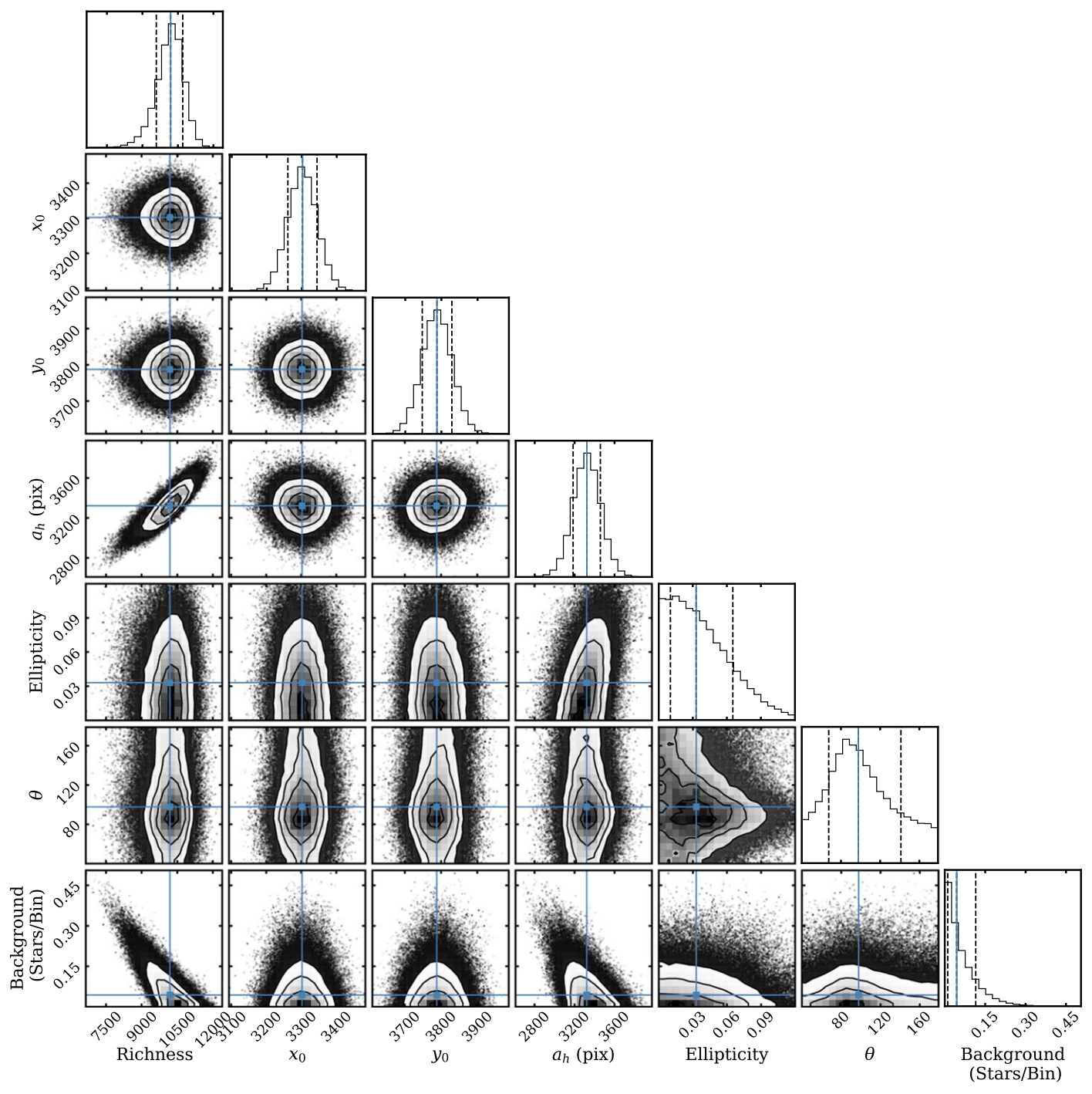


Figure 12. The posterior distributions of the seven-parameter structural fit for Sgr II using the exponential model. The three black vertical dashed lines represent the 16th, 50th, and 84th percentiles. The blue lines and markers show the median values.

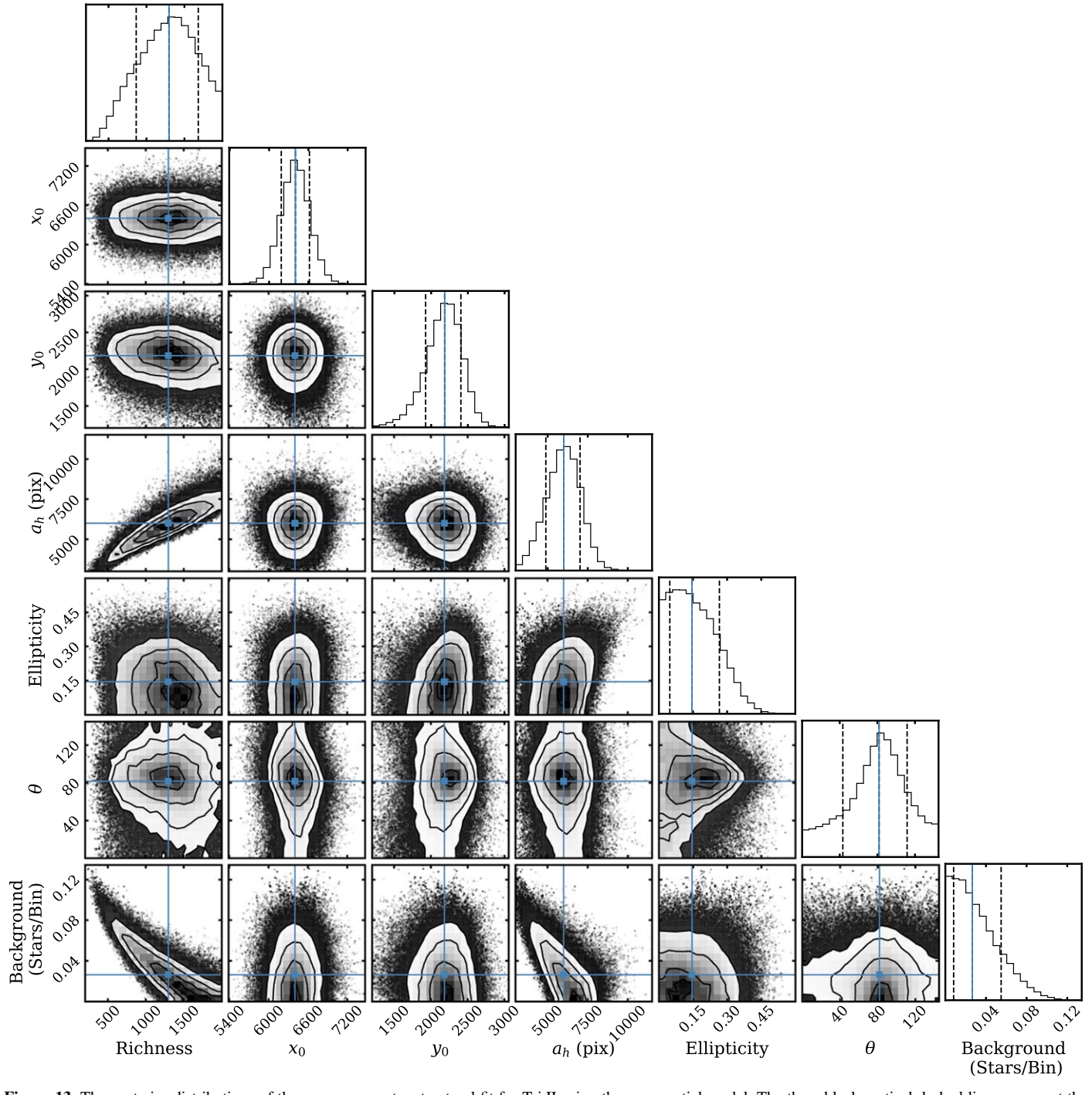


Figure 13. The posterior distributions of the seven-parameter structural fit for Tri II using the exponential model. The three black vertical dashed lines represent the 16th, 50th, and 84th percentiles. The blue lines and markers show the median values.

Appendix B References for Figure 8

We largely pulled from the compilations of Simon (2019) and McConnachie (2012; 2021 edition) for the UFD and UFD candidate parameters, but we have also included the more recently discovered satellites. Here, we list the individual references: Majewski et al. (2003), de Jong et al. (2008), Drlica-Wagner et al. (2015), Koposov et al. (2015b, 2018), Drlica-Wagner et al. (2016), Crnojević et al. (2016), Homma et al. (2016), Torrealba et al. (2016a), Torrealba et al. (2016b), Carlin et al. (2017), Luque et al. (2017), Homma et al. (2018),

Muñoz et al. (2018), Mutlu-Pakdil et al. (2018), Torrealba et al. (2018), Simon et al. (2020), Cerny et al. (2021a, 2021b, 2023b, 2023c), Ji et al. (2021), Richstein et al. (2022), and Smith et al. (2023).

The globular cluster parameters come from the compilation in Harris (2010), with newer additions from Muñoz et al. (2018) and Torrealba et al. (2019). The Harris (2010) compilation draws from the works of the following: Harris & van den Bergh (1984), Webbink (1985), Peterson & Reed (1987), van den Bergh et al. (1991), Tucholke (1992), Mallen-Ornelas & Djorgovski (1993), Trager et al. (1993), Cote et al.

(1995), Trager et al. (1995), Harris et al. (1997), Kaisler et al. (1997), Lehmann & Scholz (1997), Ivanov et al. (2005), Kobulnicky et al. (2005), McLaughlin & van der Marel (2005), Ferraro et al. (2006), Hilker (2006), McLaughlin et al. (2006), Ortolani et al. (2006), Bellazzini (2007), Carraro et al. (2007), de Marchi & Pulone (2007), Froebrich et al. (2007), Koposov et al. (2007), Lanzoni et al. (2007a), Lanzoni et al. (2007b), Lanzoni et al. (2007c), Bonatto & Bica (2008), Kurtev et al. (2008), Carraro (2009), and Lanzoni et al. (2010).

We have also included the newer DELVE clusters from the following: Mau et al. (2020), Cerny et al. (2023b), Cerny et al. (2023a), and the faintest known MW satellite recently found by Smith et al. (2024).

ORCID iDs Hannah Richstein https://orcid.org/0000-0002-3188-2718

Nitya Kallivayalil https://orcid.org/0000-0002-3204-1742 Joshua D. Simon https://orcid.org/0000-0002-4733-4994 Christopher T. Garling https://orcid.org/0000-0001-9061-1697 Andrew Wetzel https://orcid.org/0000-0003-0603-8942 Jack T. Warfield https://orcid.org/0000-0003-1634-4644 Roeland P. van der Marel https://orcid.org/0000-0001-7827-7825 Myoungwon Jeon https://orcid.org/0000-0001-6529-9777 Jonah C. Rose https://orcid.org/0000-0002-2628-0237 Paul Torrey https://orcid.org/0000-0002-5653-0786 Anna Claire Engelhardt https://orcid.org/0009-0006-2183-9560 Gurtina Besla https://orcid.org/0000-0003-0715-2173 Yumi Choi https://orcid.org/0000-0003-1680-1884 Marla Geha https://orcid.org/0000-0002-7007-9725 Puragra Guhathakurta https://orcid.org/0000-0001-8867-4234 Evan N. Kirby https://orcid.org/0000-0001-6196-5162 Ekta Patel https://orcid.org/0000-0002-9820-1219 Elena Sacchi https://orcid.org/0000-0001-5618-0109

Sangmo Tony Sohn https://orcid.org/0000-0001-8368-0221 References

```
Abbott, T. M. C., Abdalla, F. B., Allam, S., et al. 2018, ApJS, 239, 18
Agertz, O., Pontzen, A., Read, J. I., et al. 2020, MNRAS, 491, 1656
Anderson, J., Baggett, S., & Kuhn, B. 2021, Updating the WFC3/UVIS CTE
  model and Mitigation Strategies, Instrument Science Report, 2021-9, STSI
Anderson, J., & Ryon, J. E. 2018, Improving the Pixel-Based CTE-correction
   Model for ACS/WFC, Instrument Science Report, ACS 2018-04, STSI
Applebaum, E., Brooks, A. M., Christensen, C. R., et al. 2021, ApJ, 906, 96
Astropy Collaboration, Price-Whelan, A. M., Lim, P. L., et al. 2022, ApJ,
Astropy Collaboration, Price-Whelan, A. M., Sipőcz, B. M., et al. 2018, AJ,
   156, 123
Astropy Collaboration, Robitaille, T. P., Tollerud, E. J., & Streicher, O. 2013,
      A, 558, A33
Avila, R. J., Hack, W., Cara, M., et al. 2015, in ASP Conf. Ser. 495,
   Astronomical Data Analysis Software an Systems XXIV (ADASS XXIV),
   ed. A. R. Taylor & E. Rosolowsky (San Francisco, CA: ASP), 281
Barkana, R., Haiman, Z., & Ostriker, J. P. 2001, ApJ, 558, 482
Battaglia, G., Taibi, S., Thomas, G. F., & Fritz, T. K. 2022, A&A, 657, A54
Baumgardt, H., Faller, J., Meinhold, N., McGovern-Greco, C., & Hilker, M.
  2022, MNRAS, 510, 3531
Bechtol, K., Drlica-Wagner, A., Balbinot, E., et al. 2015, ApJ, 807, 50
Behroozi, P. S., Conroy, C., & Wechsler, R. H. 2010, ApJ, 717, 379
Bellazzini, M. 2007, A&A, 473, 171
Belokurov, V., Zucker, D. B., Evans, N. W., et al. 2006, ApJL, 647, L111
Bertin, E., & Arnouts, S. 1996, A&AS, 117, 393
Besla, G., Kallivayalil, N., Hernquist, L., et al. 2007, ApJ, 668, 949
Bode, P., Ostriker, J. P., & Turok, N. 2001, ApJ, 556, 93
Bohlin, R. C. 2016, AJ, 152, 60
Bonatto, C., & Bica, E. 2008, A&A, 479, 741
```

Bonnarel, F., Fernique, P., Bienaymé, O., et al. 2000, A&AS, 143, 33

```
Bose, S., Deason, A. J., & Frenk, C. S. 2018, ApJ, 863, 123
Bovill, M. S., & Ricotti, M. 2009, ApJ, 693, 1859
Bozek, B., Fitts, A., Boylan-Kolchin, M., et al. 2019, MNRAS, 483, 4086
Bradley, L., Sipőcz, B., Robitaille, T., et al. 2020, astropy/photutils: v1.0.0,
  Zenodo, doi:10.5281/zenodo,4044744
Bressan, A., Marigo, P., Girardi, L., et al. 2012, MNRAS, 427, 127
Brook, C. B., Di Cintio, A., Knebe, A., et al. 2014, ApJL, 784, L14
Brown, T. M., Tumlinson, J., Geha, M., et al. 2014, ApJ, 796, 91
Bullock, J. S., & Boylan-Kolchin, M. 2017, ARA&A, 55, 343
Burkert, A. 2000, ApJL, 534, L143
Buttry, R., Pace, A. B., Koposov, S. E., et al. 2022, MNRAS, 514, 1706
Carlin, J. L., Garling, C. T., Peter, A. H. G., et al. 2019, ApJ, 886, 109
Carlin, J. L., Sand, D. J., Muñoz, R. R., et al. 2017, AJ, 154, 267
Carraro, G. 2009, AJ, 137, 3809
Carraro, G., Zinn, R., & Moni Bidin, C. 2007, A&A, 466, 181
Cerny, W., Drlica-Wagner, A., Li, T. S., et al. 2023a, ApJL, 953, L21
Cerny, W., Martínez-Vázquez, C. E., Drlica-Wagner, A., et al. 2023b, ApJ,
Cerny, W., Pace, A. B., Drlica-Wagner, A., et al. 2021a, ApJ, 910, 18
Cerny, W., Pace, A. B., Drlica-Wagner, A., et al. 2021b, ApJL, 920, L44
Cerny, W., Simon, J. D., Li, T. S., et al. 2023c, ApJ, 942, 111
Chambers, K. C., Magnier, E. A., Metcalfe, N., et al. 2016, arXiv:1612.05560
Chan, T. K., Kereš, D., Oñorbe, J., et al. 2015, MNRAS, 454, 2981
Chen, Y., Girardi, L., Bressan, A., et al. 2014, MNRAS, 444, 2525
Chiti, A., Frebel, A., Ji, A. P., et al. 2023, AJ, 165, 55
Chiti, A., Frebel, A., Simon, J. D., et al. 2021, NatAs, 5, 392
Christensen, C. R., Brooks, A., Munshi, F., et al. 2024, ApJ, 961, 236
Correa Magnus, L., & Vasiliev, E. 2022, MNRAS, 511, 2610
Cote, P., Welch, D. L., Fischer, P., & Gebhardt, K. 1995, ApJ, 454, 788
Crnojević, D., Sand, D. J., Zaritsky, D., et al. 2016, ApJL, 824, L14
Davé, R., Spergel, D. N., Steinhardt, P. J., & Wandelt, B. D. 2001, ApJ,
  547, 574
Dawoodbhoy, T., Shapiro, P. R., Ocvirk, P., et al. 2018, MNRAS, 480,
de Jong, J. T. A., Harris, J., Coleman, M. G., et al. 2008, ApJ, 680, 1112
de Marchi, G., & Pulone, L. 2007, A&A, 467, 107
Deason, A. J., Bose, S., Fattahi, A., et al. 2022, MNRAS, 511, 4044
Drlica-Wagner, A., Bechtol, K., Allam, S., et al. 2016, ApJL, 833, L5
Drlica-Wagner, A., Bechtol, K., Mau, S., et al. 2020, ApJ, 893, 47
Drlica-Wagner, A., Bechtol, K., Rykoff, E. S., et al. 2015, ApJ, 813, 109
Dutton, A. A., Macciò, A. V., Dekel, A., et al. 2016, MNRAS, 461, 2658
El-Badry, K., Quataert, E., Wetzel, A., et al. 2018, MNRAS, 473, 1930
Erkal, D., & Belokurov, V. A. 2020, MNRAS, 495, 2554
Ferraro, F. R., Sollima, A., Rood, R. T., et al. 2006, ApJ, 638, 433
Filion, C., & Wyse, R. F. G. 2021, ApJ, 923, 218
Fitts, A., Boylan-Kolchin, M., Bozek, B., et al. 2019, MNRAS, 490, 962
Fitts, A., Boylan-Kolchin, M., Elbert, O. D., et al. 2017, MNRAS, 471, 3547
Flores, R. A., & Primack, J. R. 1994, ApJL, 427, L1
Ford, H. C., Bartko, F., Bely, P. Y., et al. 1998, Proc. SPIE, 3356, 234
Foreman-Mackey, D. 2016, JOSS, 1, 24
Foreman-Mackey, D., Hogg, D. W., Lang, D., & Goodman, J. 2013, PASP,
  125, 306
Frenk, C. S., White, S. D. M., Davis, M., & Efstathiou, G. 1988, ApJ, 327, 507
Fritz, T. K., Carrera, R., Battaglia, G., & Taibi, S. 2019, A&A, 623, A129
Froebrich, D., Meusinger, H., & Scholz, A. 2007, MNRAS, 377, L54
Fruchter, A. S., & Hook, R. N. 2002, PASP, 114, 144
Fu, S. W., Weisz, D. R., Starkenburg, E., et al. 2023, ApJ, 958, 167
Gaia Collaboration, Brown, A. G. A., Vallenari, A., et al. 2021, A&A, 649, A1
Gaia Collaboration, Prusti, T., de Bruijne, J. H. J., et al. 2016, A&A, 595, A1
Garling, C. T., Peter, A. H. G., Kochanek, C. S., Sand, D. J., & Crnojević, D.
  2020, MNRAS, 492, 1713
Garrison-Kimmel, S., Boylan-Kolchin, M., Bullock, J. S., & Lee, K. 2014,
      VRAS, 438, 2578
Garrison-Kimmel, S., Bullock, J. S., Boylan-Kolchin, M., & Bardwell, E.
  2017, MNRAS, 464, 3108
Gelato, S., & Sommer-Larsen, J. 1999, MNRAS, 303, 321
Genel, S., Nelson, D., Pillepich, A., et al. 2018, MNRAS, 474, 3976
Goater, A., Read, J. I., Noël, N. E. D., et al. 2024, MNRAS, 527, 2403
Green, G. 2018, JOSS, 3, 695
Gutcke, T. A., Pfrommer, C., Bryan, G. L., et al. 2022, ApJ, 941, 120
Harris, C. R., Millman, K. J., van der Walt, S. J., et al. 2020, Natur, 585, 357
Harris, W. E. 2010, arXiv:1012.3224
Harris, W. E. 2018, AJ, 156, 296
Harris, W. E., Bell, R. A., Vandenberg, D. A., et al. 1997, AJ, 114, 1030
Harris, W. E., & van den Bergh, S. 1984, AJ, 89, 1816
Hilker, M. 2006, A&A, 448, 171
Hogan, C. J., & Dalcanton, J. J. 2000, PhRvD, 62, 063511
```

```
Homma, D., Chiba, M., Okamoto, S., et al. 2016, ApJ, 832, 21
Homma, D., Chiba, M., Okamoto, S., et al. 2018, PASJ, 70, S18
Hopkins, P. F., Wetzel, A., Kereš, D., et al. 2018, MNRAS, 480, 800
Hunter, J. D. 2007, CSE, 9, 90
Ivanov, V. D., Kurtev, R., & Borissova, J. 2005, A&A, 442, 195
Ivezić, Ž, Kahn, S. M., Tyson, J. A., et al. 2019, ApJ, 873, 111
Jahn, E. D., Sales, L. V., Wetzel, A., et al. 2022, MNRAS, 513, 2673
Jensen, J., Hayes, C. R., Sestito, F., et al. 2024, MNRAS, 527, 4209
Jeon, M., Besla, G., & Bromm, V. 2017, ApJ, 848, 85
Jeon, M., Besla, G., & Bromm, V. 2021a, MNRAS, 506, 1850
Jeon, M., Bromm, V., Besla, G., Yoon, J., & Choi, Y. 2021b, MNRAS, 502, 1
Jethwa, P., Erkal, D., & Belokurov, V. 2016, MNRAS, 461, 2212
Ji, A. P., Koposov, S. E., Li, T. S., et al. 2021, ApJ, 921, 32
Ji, A. P., Simon, J. D., Frebel, A., Venn, K. A., & Hansen, T. T. 2019, ApJ,
Ji, A. P., Simon, J. D., Roederer, I. U., et al. 2023, AJ, 165, 100
Kaisler, D., Harris, W. E., & McLaughlin, D. E. 1997, PASP, 109, 920
Kallivayalil, N., Sales, L. V., Zivick, P., et al. 2018, ApJ, 867, 19
Kallivayalil, N., van der Marel, R. P., Besla, G., Anderson, J., & Alcock, C.
   2013, ApJ, 764, 161
Kim, D., & Jerjen, H. 2015, ApJL, 808, L39
Kim, J., Jeon, M., Choi, Y., et al. 2023, ApJ, 959, 31
Kirby, E. N., Cohen, J. G., Simon, J. D., & Guhathakurta, P. 2015a, ApJL,
Kirby, E. N., Cohen, J. G., Simon, J. D., et al. 2017, ApJ, 838, 83
Kirby, E. N., Simon, J. D., & Cohen, J. G. 2015b, ApJ, 810, 56
Kluyver, T., Ragan-Kelley, B., Pérez, F., et al. 2016, in Positioning and Power
   in Academic Publishing: Players, Agents and Agendas, ed. F. Loizides &
   B. Scmidt (Amsterdam: IOS Press), 87
Kobulnicky, H. A., Monson, A. J., Buckalew, B. A., et al. 2005, AJ, 129, 239
Koposov, S., de Jong, J. T. A., Belokurov, V., et al. 2007, ApJ, 669, 337
Koposov, S. E., Belokurov, V., Torrealba, G., & Evans, N. W. 2015a, ApJ,
   805, 130
Koposov, S. E., Casey, A. R., Belokurov, V., et al. 2015b, ApJ, 811, 62
Koposov, S. E., Walker, M. G., Belokurov, V., et al. 2018, MNRAS, 479, 5343
Kroupa, P. 2001, MNRAS, 322, 231
Kurtev, R., Ivanov, V. D., Borissova, J., & Ortolani, S. 2008, A&A, 489, 583
Laevens, B. P. M., Martin, N. F., Bernard, E. J., et al. 2015a, ApJ, 813, 44
Laevens, B. P. M., Martin, N. F., Ibata, R. A., et al. 2015b, ApJL, 802, L18
Lanzoni, B., Dalessandro, E., Ferraro, F. R., et al. 2007a, ApJ, 663, 267
Lanzoni, B., Dalessandro, E., Ferraro, F. R., et al. 2007b, ApJL, 668, L139
Lanzoni, B., Ferraro, F. R., Dalessandro, E., et al. 2010, ApJ, 717, 653
Lanzoni, B., Sanna, N., Ferraro, F. R., et al. 2007c, ApJ, 663, 1040
Lazar, A., Bullock, J. S., Boylan-Kolchin, M., et al. 2020, MNRAS, 497, 2393
Lehmann, I., & Scholz, R. D. 1997, A&A, 320, 776
Longeard, N., Jablonka, P., Arentsen, A., et al. 2022, MNRAS, 516, 2348
Longeard, N., Jablonka, P., Battaglia, G., et al. 2023, MNRAS, 525, 3086
Longeard, N., Martin, N., Ibata, R. A., et al. 2021, MNRAS, 503, 2754
Longeard, N., Martin, N., Starkenburg, E., et al. 2020, MNRAS, 491, 356
Lovell, M. R., Eke, V., Frenk, C. S., et al. 2012, MNRAS, 420, 2318
Luque, E., Pieres, A., Santiago, B., et al. 2017, MNRAS, 468, 97
Macciò, A. V., Frings, J., Buck, T., et al. 2017, MNRAS, 472, 2356
Macciò, A. V., Frings, J., Buck, T., et al. 2019, MNRAS, 484, 5400
Macciò, A. V., Paduroiu, S., Anderhalden, D., Schneider, A., & Moore, B.
   2012, MNRAS, 424, 1105
Madau, P., & Dickinson, M. 2014, ARA&A, 52, 415
Majewski, S. R., Skrutskie, M. F., Weinberg, M. D., & Ostheimer, J. C. 2003,
     nJ. 599, 1082
Mallen-Ornelas, G., & Djorgovski, S. 1993, in ASP Conf. Ser. 50, Structure
   and Dynamics of Globular Clusters, ed. S. G. Djorgovski & G. Meylan (San
   Francisco, CA: ASP), 313
Manwadkar, V., & Kravtsov, A. V. 2022, MNRAS, 516, 3944
Marigo, P., Girardi, L., Bressan, A., et al. 2017, ApJ, 835, 77
Martin, N. F., de Jong, J. T. A., & Rix, H.-W. 2008, ApJ, 684, 1075
Martin, N. F., Ibata, R. A., Collins, M. L. M., et al. 2016, ApJ, 818, 40
Martin, N. F., Nidever, D. L., Besla, G., et al. 2015, ApJL, 804, L5
Martínez-Vázquez, C. E., Vivas, A. K., Gurevich, M., et al. 2019, MNRAS,
   490, 2183
Mau, S., Cerny, W., Pace, A. B., et al. 2020, ApJ, 890, 136
McConnachie, A. W. 2012, AJ, 144, 4
McConnachie, A. W., & Venn, K. A. 2020, AJ, 160, 124
McLaughlin, D. E., Anderson, J., Meylan, G., et al. 2006, ApJS, 166, 249
McLaughlin, D. E., & van der Marel, R. P. 2005, ApJS, 161, 304
Medina, J., Mack, J., & Calamida, A. 2022, WFC3/UVIS Encircled Energy,
   Instrument Science Report, WFC3 2022-2, STSI
Miyazaki, S., Komiyama, Y., Kawanomoto, S., et al. 2018, PASJ, 70, S1
```

```
Moore, B. 1994, Natur, 370, 629
Morrison, J. E. 1995, in ASP Conf. Ser. 77, Astronomical Data Analysis
  Software and Systems IV, ed. R. A. Shaw, H. E. Payne, & J. J. E. Hayes
  (San Francisco, CA: ASP), 179
Moskowitz, A. G., & Walker, M. G. 2020, ApJ, 892, 27
Muñoz, R. R., Côté, P., Santana, F. A., et al. 2018, ApJ, 860, 66
Muñoz, R. R., Padmanabhan, N., & Geha, M. 2012, ApJ, 745, 127
Munshi, F., Brooks, A. M., Applebaum, E., et al. 2021, ApJ, 923, 35
Mutlu-Pakdil, B., Sand, D. J., Carlin, J. L., et al. 2018, ApJ, 863, 25
Mutlu-Pakdil, B., Sand, D. J., Crnojević, D., et al. 2020, ApJ, 902, 106
Mutlu-Pakdil, B., Sand, D. J., Crnojević, D., et al. 2021, ApJ, 918, 88
Mutlu-Pakdil, B., Sand, D. J., Walker, M. G., et al. 2019, ApJ, 885, 53
Nagarajan, P., Weisz, D. R., & El-Badry, K. 2022, ApJ, 932, 19
Nagasawa, D. Q., Marshall, J. L., Li, T. S., & Hansen, T. T. 2018, ApJ, 852, 99
Navarro, J. F., Eke, V. R., & Frenk, C. S. 1996, MNRAS, 283, L72
Newton, O., Di Cintio, A., Cardona-Barrero, S., et al. 2023, ApJL, 946, L37
Nidever, D. L., Olsen, K., Choi, Y., et al. 2021, AJ, 161, 74
Nidever, D. L., Olsen, K., Walker, A. R., et al. 2017, AJ, 154, 199
Ocvirk, P., Aubert, D., Sorce, J. G., et al. 2020, MNRAS, 496, 4087
Oh, S.-H., Brook, C., Governato, F., et al. 2011, AJ, 142, 24
Orkney, M. D. A., Read, J. I., Rey, M. P., et al. 2021, MNRAS, 504, 3509
Ortolani, S., Bica, E., & Barbuy, B. 2006, ApJL, 646, L115
Ou, X., Chiti, A., Shipp, N., et al. 2024, ApJ, 966, 33
Pace, A. B., Erkal, D., & Li, T. S. 2022, ApJ, 940, 136
Patel, E., Kallivayalil, N., Garavito-Camargo, N., et al. 2020, ApJ, 893, 121
Pearson, S., Starkenburg, T. K., Johnston, K. V., et al. 2019, ApJ, 883, 87
Pedregosa, F., Varoquaux, G., Gramfort, A., et al. 2011, Journal of Machine
  Learning Research, 12, 2825
Peebles, P. J. E. 1984, ApJ, 277, 470
Peterson, C. J., & Reed, B. C. 1987, PASP, 99, 20
Pillepich, A., Springel, V., Nelson, D., et al. 2018, MNRAS, 473, 4077
Plummer, H. C. 1911, MNRAS, 71, 460
Pontzen, A., & Governato, F. 2012, MNRAS, 421, 3464
Prgomet, M., Rey, M. P., Andersson, E. P., et al. 2022, MNRAS, 513, 2326
Racca, G. D., Laureijs, R., Stagnaro, L., et al. 2016, Proc. SPIE, 9904, 990400
Read, J. I., & Gilmore, G. 2005, MNRAS, 356, 107
Read, J. I., Iorio, G., Agertz, O., & Fraternali, F. 2017, MNRAS, 467, 2019
Revaz, Y. 2023, A&A, 679, A2
Revaz, Y., & Jablonka, P. 2018, A&A, 616, A96
Rey, M. P., Pontzen, A., Agertz, O., et al. 2020, MNRAS, 497, 1508
Rey, M. P., Pontzen, A., Agertz, O., et al. 2022, MNRAS, 511, 5672
Richstein, H., Patel, E., Kallivayalil, N., et al. 2022, ApJ, 933, 217
Robles, V. H., Bullock, J. S., Elbert, O. D., et al. 2017, MNRAS, 472, 2945
Rocha, M., Peter, A. H. G., & Bullock, J. 2012, MNRAS, 425, 231
Rocha, M., Peter, A. H. G., Bullock, J. S., et al. 2013, MNRAS, 430, 81
Rosdahl, J., Blaizot, J., Aubert, D., Stranex, T., & Teyssier, R. 2013, MNRAS,
  436, 2188
Rosdahl, J., & Teyssier, R. 2015, MNRAS, 449, 4380
Rose, J. C., Torrey, P., Vogelsberger, M., & O'Neil, S. 2023, MNRAS,
  519, 5623
Sacchi, E., Richstein, H., Kallivayalil, N., et al. 2021, ApJL, 920, L19
Sales, L. V., Navarro, J. F., Kallivayalil, N., & Frenk, C. S. 2017, MNRAS,
  465, 1879
Sales, L. V., Wetzel, A., & Fattahi, A. 2022, NatAs, 6, 897
Sanati, M., Jeanquartier, F., Revaz, Y., & Jablonka, P. 2023, A&A, 669, A94
Sand, D. J., Olszewski, E. W., Willman, B., et al. 2009, ApJ, 704, 898
Sand, D. J., Strader, J., Willman, B., et al. 2012, ApJ, 756, 79
Santistevan, I. B., Wetzel, A., Tollerud, E., Sanderson, R. E., & Samuel, J.
  2023, MNRAS, 518, 1427
Schlafly, E. F., & Finkbeiner, D. P. 2011, ApJ, 737, 103
Schlegel, D. J., Finkbeiner, D. P., & Davis, M. 1998, ApJ, 500, 525
Sestito, F., Roediger, J., Navarro, J. F., et al. 2023a, MNRAS, 523, 123
Sestito, F., Zaremba, D., Venn, K. A., et al. 2023b, MNRAS, 525, 2875
Shao, S., Gao, L., Theuns, T., & Frenk, C. S. 2013, MNRAS, 430, 2346
Simon, J., Fu, S. W., Geha, M., Kelson, D. D., & Alarcon Jara, A. G. 2019,
   AAS Meeting Abstracts, 233, 449.04
Simon, J. D. 2019, ARA&A, 57, 375
Simon, J. D., Brown, T. M., Drlica-Wagner, A., et al. 2021, ApJ, 908, 18
Simon, J. D., Drlica-Wagner, A., Li, T. S., et al. 2015, ApJ, 808, 95
Simon, J. D., & Geha, M. 2007, ApJ, 670, 313
Simon, J. D., Li, T. S., Erkal, D., et al. 2020, ApJ, 892, 137
Sirianni, M., Jee, M. J., Benítez, N., et al. 2005, PASP, 117, 1049
Smith, S. E. T., Cerny, W., Hayes, C. R., et al. 2024, ApJ, 961, 92
Smith, S. E. T., Jensen, J., Roediger, J., et al. 2023, AJ, 166, 76
Sommer-Larsen, J., & Dolgov, A. 2001, ApJ, 551, 608
Sorce, J. G., Ocvirk, P., Aubert, D., et al. 2022, MNRAS, 515, 2970
```

```
Spergel, D., Gehrels, N., Baltay, C., et al. 2015, arXiv:1503.03757
Springel, V. 2005, MNRAS, 364, 1105
Stetson, P. B. 1987, PASP, 99, 191
```

- Stetson, P. B. 1992, in ASP Conf. Ser. 25, Astronomical Data Analysis Software and Systems I, ed. D. M. Worrall, C. Biemesderfer, & J. Barnes (San Francisco, CA: ASP), 297
- STScI Development Team 2012, DrizzlePac: HST image software, Astrophysics Source Code Library, ascl:1212.011
- STScI Development Team 2018, synphot: Synthetic photometry using Astropy, Astrophysics Source Code Library, ascl:1811.001
- STScI Development Team 2020, stsynphot: synphot for HST and JWST, Astrophysics Source Code Library, ascl:2010.003
- Tarumi, Y., Yoshida, N., & Frebel, A. 2021, ApJL, 914, L10
- Tau, E. A., Vivas, A. K., & Martínez-Vázquez, C. E. 2024, AJ, 167, 57 Teyssier, R. 2002, A&A, 385, 337
- Torrealba, G., Belokurov, V., Koposov, S. E., et al. 2018, MNRAS, 475, 5085 Torrealba, G., Belokurov, V., & Koposov, S. E. 2019, MNRAS, 484, 2181
- Torrealba, G., Koposov, S. E., Belokurov, V., & Irwin, M. 2016a, MNRAS, 459, 2370
- Torrealba, G., Koposov, S. E., Belokurov, V., et al. 2016b, MNRAS, 463, 712 Trager, S. C., Djorgovski, S., & King, I. R. 1993, in ASP Conf. Ser. 50, Structure and Dynamics of Globular Clusters, ed. S. G. Djorgovski & G. Meylan (San Francisco, CA: ASP), 347
- Trager, S. C., King, I. R., & Djorgovski, S. 1995, AJ, 109, 218 Tucholke, H. J. 1992, A&A, 264, 513

- Tulin, S., & Yu, H.-B. 2018, PhR, 730, 1 van den Bergh, S., Morbey, C., & Pazder, J. 1991, ApJ, 375, 594 Venn, K. A., Starkenburg, E., Malo, L., Martin, N., & Laevens, B. P. M. 2017, MNRAS, 466, 3741
- Virtanen, P., Gommers, R., Oliphant, T. E., et al. 2020, NatMe, 17, 261 Vogelsberger, M., Zavala, J., Cyr-Racine, F.-Y., et al. 2016, MNRAS, 460, 1399
- Walker, M. G., Mateo, M., Olszewski, E. W., et al. 2015, ApJ, 808, 108 Walker, M. G., Mateo, M., Olszewski, E. W., et al. 2016, ApJ, 819, 53
- Waller, F., Venn, K. A., Sestito, F., et al. 2023, MNRAS, 519, 1349
- Wang, L., Dutton, A. A., Stinson, G. S., et al. 2015, MNRAS, 454, 83 Webbink, R. F. 1985, in Dynamics of Star Clusters, ed. J. Goodman & P. Hut
- (Cambridge: Cambridge Univ. Press), 541 Wechsler, R. H., Bullock, J. S., Primack, J. R., Kravtsov, A. V., & Dekel, A.
- 2002, ApJ, 568, 52 Weisz, D. R., Dolphin, A. E., Skillman, E. D., et al. 2014, ApJ, 789, 147
- Wetzel, A., Hayward, C. C., Sanderson, R. E., et al. 2023, ApJS, 265, 44
- Wetzel, A. R., Deason, A. J., & Garrison-Kimmel, S. 2015, ApJ, 807, 49
- Wheeler, C., Hopkins, P. F., Pace, A. B., et al. 2019, MNRAS, 490, 4447 White, S. D. M., & Rees, M. J. 1978, MNRAS, 183, 341
- Willman, B., Blanton, M. R., West, A. A., et al. 2005, AJ, 129, 2692
- Willman, B., & Strader, J. 2012, AJ, 144, 76
- Wolf, J., Martinez, G. D., Bullock, J. S., et al. 2010, MNRAS, 406, 1220 Yang, Y., Hammer, F., Jiao, Y., & Pawlowski, M. S. 2022, MNRAS, 512, 4171